

1 Postprint of: Kulpa A., Ryl J., Schroeder G., Koterwa A., Sein Anand J., Ossowski T.,
2 Niedzialkowski P., Simultaneous voltammetric determination of Cd²⁺, Pb²⁺, and Cu²⁺ ions
3 captured by Fe₃O₄@SiO₂ core-shell nanostructures of various outer amino chain length,
4 Journal of Molecular Liquids, Vol. 314 (2020), 113677, DOI: [10.1016/j.molliq.2020.113677](https://doi.org/10.1016/j.molliq.2020.113677)

5
6 © 2020. This manuscript version is made available under the CC-BY-NC-ND 4.0
7 license <http://creativecommons.org/licenses/by-nc-nd/4.0/>

8
9 **Simultaneous voltammetric determination of Cd²⁺, Pb²⁺, and Cu²⁺**
10 **ions captured by Fe₃O₄@SiO₂ core-shell nanostructures of various**
11 **outer amino chain length**
12

13 A. Kulpa¹, J. Ryl², G. Schroeder³, A. Koterwa¹, J. Sein Anand^{4,5}, T. Ossowski¹,
14 P. Niedzialkowski^{1*}

15 ¹ Department of Analytical Chemistry, Faculty of Chemistry, University of Gdansk, Wita
16 Stwosza Str. 63, 80-308 Gdansk, Poland

17 ² Department of Electrochemistry, Corrosion and Materials Engineering, Faculty of Chemistry,
18 Gdansk University of Technology, Narutowicza 11/12, 80-233 Gdansk, Poland

19 ³ Faculty of Chemistry, Adam Mickiewicz University in Poznan, Uniwersytetu Poznańskiego
20 Str. 8, 61-614 Poznan, Poland

21 ⁴ Department of Clinical Toxicology, Medical University of Gdansk, 4/6 Kartuska St., 80-104
22 Gdansk, Poland

23 ⁵ Pomeranian Center of Clinical Toxicology, 4/6 Kartuska St., 80-104 Gdansk, Poland

24
25
26 *corresponding author: Pawel Niedzialkowski

27 e-mail address: pawel.niedzialkowski@ug.edu.pl

28 tel: +48 58 523 51 00

30 **Abstract**

31 In the present study, we examined a novel functionalised magnetic nanoparticles
32 $\text{Fe}_3\text{O}_4@\text{SiO}_2\text{-N}_n$ as a nano adsorbent for binding of Cd^{2+} , Pb^{2+} , Cu^{2+} ions in an aqueous solution.
33 First, we obtained the nanoparticles functionalised with various carbon chains containing
34 different number of amino groups: (3-amino)propyltriethoxysilane ($\text{Fe}_3\text{O}_4@\text{SiO}_2\text{-N}_1$),
35 N-(2-aminoethyl)-3-aminopropyltrimethoxysilane ($\text{Fe}_3\text{O}_4@\text{SiO}_2\text{-N}_2$) and
36 N^1 -(3-trimethoxysilylpropyl)diethylenetriamine ($\text{Fe}_3\text{O}_4@\text{SiO}_2\text{-N}_3$). In the next step, we
37 conducted their characterisation using SEM, TEM, FT-IR, and XPS methods.

38 The detection of Cd^{2+} , Pb^{2+} , Cu^{2+} metal ions was performed under optimised
39 experimental conditions using DPASV and HDME techniques. Using these methods we
40 conducted the Cd^{2+} , Pb^{2+} , Cu^{2+} binding comparison in 4.5 μM concentration with 4 mg of
41 $\text{Fe}_3\text{O}_4@\text{SiO}_2\text{-N}_n$. Obtained results show that the adsorption rate of each ion differs due to the
42 nanoparticles modification.

43 The highest Pb^{2+} binding capacity was achieved using $\text{Fe}_3\text{O}_4@\text{SiO}_2\text{-N}_1$ and
44 $\text{Fe}_3\text{O}_4@\text{SiO}_2\text{-N}_2$. The smallest binding capacity was observed for Cd^{2+} ions by
45 $\text{Fe}_3\text{O}_4@\text{SiO}_2\text{-N}_2$ and $\text{Fe}_3\text{O}_4@\text{SiO}_2\text{-N}_1$.

46 The Cd^{2+} binding was not observed for both $\text{Fe}_3\text{O}_4@\text{SiO}_2\text{-N}_2$ and $\text{Fe}_3\text{O}_4@\text{SiO}_2\text{-N}_3$
47 nanoparticles. Additionally, Pb^{2+} was not bound by $\text{Fe}_3\text{O}_4@\text{SiO}_2\text{-N}_3$. The research results show
48 that the $\text{Fe}_3\text{O}_4@\text{SiO}_2\text{-N}_3$ nanoparticles bind copper ions with high selectivity.

49 For the first time we performed the adsorption-desorption experiments using DPASV to
50 prove the Cu^{2+} binding activity of $\text{Fe}_3\text{O}_4@\text{SiO}_2\text{-N}_3$ nanoparticles. Obtained results indicate that
51 examined nanoparticles show strong binding capability. Additionally, we obtained 99.9 %
52 recovery of Cu^{2+} ions.

53
54
55 **Keywords:** Fe_3O_4 nanoparticles; amino-modified $\text{Fe}_3\text{O}_4@\text{SiO}_2$ nanostructures; cadmium, lead
56 and copper ions removal, copper adsorption-desorption experiment
57
58

59 1. Introduction

60 In the last few decades we observed increasing heavy metal pollution generated by
61 human activity - manufacturing processes such as refining and use of fertiliser and pesticides.
62 Heavy metals have caused serious environmental concerns due to their low biodegradability,
63 bioaccumulation tendency and mutagenicity [1,2]. Many heavy metals are regarded as
64 carcinogens [3]. Due to the dissemination of lead in the environment and its increasing usage
65 in industry, its carcinogenicity has been an object of interest of many research projects. Based
66 on the experimental carcinogenicity results, the International Agency for Research on Cancer
67 (IARC) commission classified lead and inorganic lead derivatives in 2B group, considered as
68 possible carcinogenic to humans [4], while cadmium is classified as a human carcinogen [5].
69 Lead does not cause cancer, but it can contribute to its development [6,7]. Cadmium causes
70 cancer by multiple mechanism based on, among others, inhibition of DNA damage repair and
71 oxidative stress [5]. Recycling of heavy metals from wastewater has become essential field of
72 scientific research and industry.

73 In recent years scientists utilised many metal ion separation and removal methods,
74 including chemical co-precipitation [8], chemical coagulation process [9], flotation [10,11] and
75 microflotation [12] techniques, ion removal by membrane filtration [13], osmosis [14],
76 extraction with ionic liquids [15]. Adsorption methods predominate over traditional separation
77 techniques due to their simplicity, easy handling and sludge-free operation, regeneration
78 capacity, and cost-effectiveness [16]. Many metal ion adsorbents are known, including pumice
79 [17], composite mineral adsorbents [18], pectin-based adsorbents [19], organic frameworks
80 [20], and carbonaceous materials, such as activated carbon [21], biochar [22], carbon nanotubes
81 [23], and graphene oxide [24].

82 Nowadays, the most popular agents for wastewater ion removal are the
83 superparamagnetic modified nanoparticle adsorbents based on iron oxide Fe_3O_4 — imprinted
84 magnetic biosorbent [25], copolymerized polyacrylamide cellulose modified nanomagnetite
85 [26], sulfone-modified magnetic activated carbon for Cd^{2+} , Pb^{2+} , and As^{3+} removal [27], and
86 many magnetic materials used for dye remediation [28–30]. The superparamagnetic Fe_3O_4
87 nanoparticles with functionalised surface adsorbent have been successfully applied to remove
88 variety of wastewater heavy metal ions, such as copper, zinc, mercury, chromium, lead,
89 cadmium, manganese, uranium, or silver [31–35]. Among adsorbents utilised to remove both
90 organic and inorganic wastewater compounds, magnetic nanoparticles with large surface area,
91 facile maintenance, and high efficiency took a special place due to the simple, convenient, and
92 fast separation using external magnetic field [36–40]. In comparison with the traditional solvent

93 extraction, these superparamagnetic modified nanoparticle adsorption methods are more
94 economic, more cost-effective, and environmentally friendly [41]. Many research groups
95 focused on the amino-functionalised $\text{Fe}_3\text{O}_4@\text{SiO}_2$ core-shell magnetic nanocomposites as a
96 novel adsorbent for the removal of aqueous pollutants [42,43].

97 Metals like, among others, gadolinium, technetium, iron, manganese, cobalt, gallium,
98 play a crucial role in medicine. These elements are widely used in diagnostic procedures as, for
99 example, radioisotope or contrast agents. Additionally, platinum, gold, silver, lithium, zinc,
100 iron, or bismuth may also be used in a treatment of various diseases [44].

101 Metals can also be extremely toxic and cause life-threatening illnesses [45]. One of the
102 most frequently occurring disease is Wilson's disease.

103 Wilson's disease is a rare, autosomal recessive, and lethal-without-treatment genetic
104 disorder caused by the excessive copper storage in various body tissues. In the case of healthy
105 individuals, we can observe a balance between intestinal absorption of dietary copper and its
106 hepatic excretion in bile. In Wilson's disease, hepatic copper is neither excreted in bile, nor
107 incorporated into ceruloplasmin. This abnormality causes the accumulation of copper to toxic
108 levels and its storage mainly in liver, brain, and cornea. The signs of Wilson's disease are as-
109 sociated with liver diseases and neurological symptoms. The diagnosis is based on the elevated
110 urinary and hepatic copper and low ceruloplasmin levels. Management of Wilson's disease in-
111 volves decreasing the excess levels of copper, chelation therapy, and oral zinc therapy. In some
112 cases, liver transplantation may be necessary [46].

113 In this work, a series of silica-coated superparamagnetic $\text{Fe}_3\text{O}_4@\text{SiO}_2$ core-shell
114 nanoparticles with modified surfaces differing in the number of amino groups in outer chains
115 — $\text{Fe}_3\text{O}_4@\text{SiO}_2\text{-N}_1$, $\text{Fe}_3\text{O}_4@\text{SiO}_2\text{-N}_2$, $\text{Fe}_3\text{O}_4@\text{SiO}_2\text{-N}_3$ — (see, Figure 1) was synthesised. The
116 characterisation of the obtained structures was performed using SEM, TEM, FT-IR, and XPS
117 method. Subsequently, the capability of functionalised nanoparticles concerning simultaneous
118 Cd^{2+} , Pb^{2+} , and Cu^{2+} ion binding was studied using electrochemical techniques, such as DPV
119 in combination with HMDE and preconcentration method. Finally, the adsorption-desorption
120 experiments using DPASV method were performed for the first time to examine the Cu^{2+}
121 binding by $\text{Fe}_3\text{O}_4@\text{SiO}_2\text{-N}_3$ nanoparticles in an aqueous solution.

122



123 2. Experimental

124 2.1. Reagents

125 All reagents, analytical grade, were purchased from the indicated suppliers and used
126 without further purification. Aqueous solutions were prepared using ultra-pure deionised water.
127 Ferric chloride hexahydrate ($\text{FeCl}_3 \cdot 6\text{H}_2\text{O}$) and ferrous chloride tetrahydrate ($\text{FeCl}_2 \cdot 4\text{H}_2\text{O}$),
128 ammonia (25%), tetraethyl orthosilicate (98 %) (TEOS), 3-(aminopropyl)triethoxysilane
129 (APTES) (99 %), N-(2-aminoethyl)-3-aminopropyltrimethoxysilane and
130 N^1 -(3-trimethoxysilylpropyl)diethylenetriamine were purchased from Sigma-Aldrich (Poland).
131 The organic solvents, potassium chloride KCl (99.9 %), cadmium nitrate tetrahydrate
132 $\text{Cd}(\text{NO}_3)_2 \cdot 4\text{H}_2\text{O}$ (99.9 %), lead nitrate $\text{Pb}(\text{NO}_3)_2$, and copper nitrate trihydrate $\text{Cu}(\text{NO}_3)_2 \cdot 3\text{H}_2\text{O}$
133 (99.9 %) were purchased from POCh (Poland).

134

135 2.2. Synthesis of Fe_3O_4

136 Fe_3O_4 nanoparticles were obtained by the coprecipitation method in an aqueous solution
137 according to the procedure described by Panta et al. [47]. The reaction was performed in non-
138 oxidising conditions maintaining the precise 1 to 2 molar ratio of $\text{Fe}^{2+}/\text{Fe}^{3+}$ in an alkaline
139 solution. The advantages and disadvantages of the synthesis reducing conditions were
140 previously described by Kim [48]. The Fe_3O_4 nanoparticles were obtained by dissolving
141 10.81 g (0.04 mol) of $\text{FeCl}_3 \cdot 6\text{H}_2\text{O}$ and 3.98 g (0.02 mol) of $\text{FeCl}_2 \cdot 4\text{H}_2\text{O}$ in 50 mL of deionised
142 water. Next, argon was passed through the vigorously stirred solution to eliminate oxygen and
143 then the reaction mixture was heated to 70 °C. When the set temperature was reached, 500 mL
144 of ammonium hydroxide solution was added dropwise up to pH 11, what resulted in the
145 formation of Fe_3O_4 . Obtained nanoparticles were washed with water to neutralise pH, washed
146 with methanol, and dried.

147

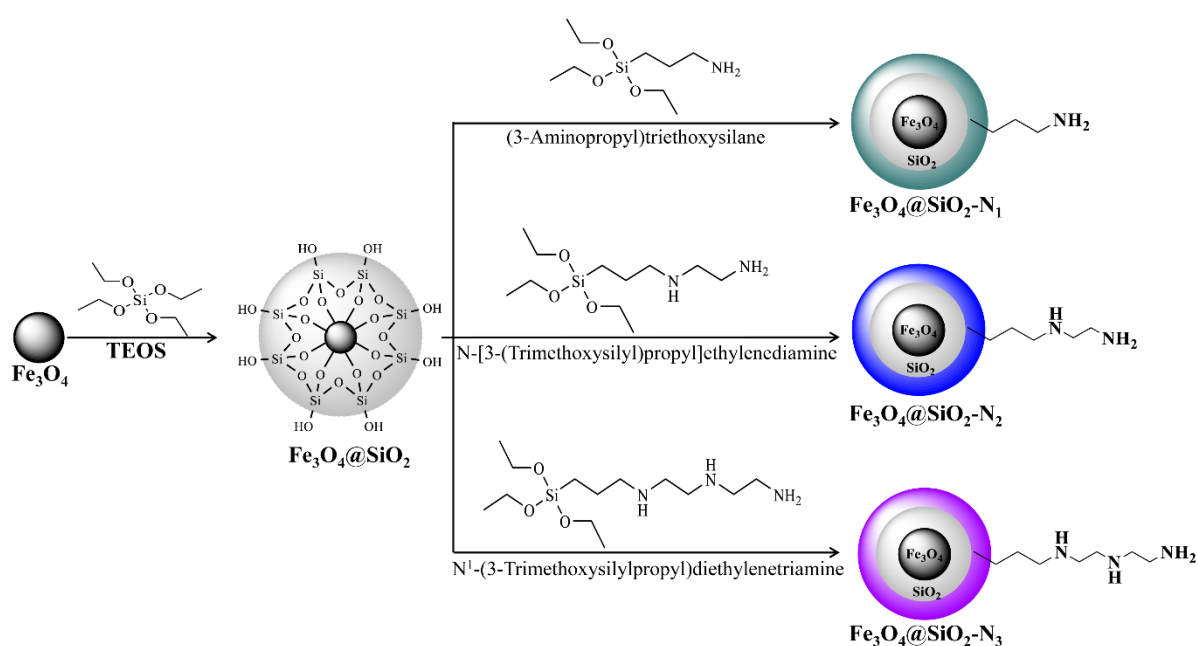
148 2.3. Synthesis of core-shell $\text{Fe}_3\text{O}_4@\text{SiO}_2$ nanoparticles

149 Synthesis of $\text{Fe}_3\text{O}_4@\text{SiO}_2$ was conducted according to Ströber procedure, which mechanism
150 and optimisation were widely described in the literature [47,49–52]. 0.1 g of Fe_3O_4
151 nanoparticles was dispersed in the mixture of ethanol and water (60:10, v/v) using an ultrasonic
152 bath for 15 min. Subsequently, 1 mL of ammonium hydroxide and 2 mL of tetraethyl
153 orthosilicate (TEOS) were added dropwise to the stirring solution at room temperature. After
154 24 h, the obtained nanoparticles were washed with water and ethanol and dried in vacuum at
155 60 °C.

156

157 2.4. Modification of core-shell $\text{Fe}_3\text{O}_4@\text{SiO}_2$ nanoparticles by amine derivatives

158 The functionalisation of $\text{Fe}_3\text{O}_4@\text{SiO}_2$ nanoparticles by amine derivatives was performed in
159 anhydrous toluene [53–55] to achieve optimal surface coverage. 4 mL of 3-amino propyl-
160 triethoxysilane (APTES), N-(2-aminoethyl)-3-aminopropyl trimethoxysilane, or
161 N^1 -(3-trimethoxysilylpropyl) diethylenetriamine was added to 0.5 g of $\text{Fe}_3\text{O}_4@\text{SiO}_2$
162 nanoparticles dispersed in 100 mL of anhydrous toluene using ultrasonic bath. Then, the
163 mixture was mechanically stirred for 12 h at 90 °C. After cooling to room temperature, the
164 obtained $\text{Fe}_3\text{O}_4@\text{SiO}_2\text{-N}_n$ amino derivatives ($\text{Fe}_3\text{O}_4@\text{SiO}_2\text{-N}_1$, $\text{Fe}_3\text{O}_4@\text{SiO}_2\text{-N}_2$, or
165 $\text{Fe}_3\text{O}_4@\text{SiO}_2\text{-N}_3$) were magnetically collected, washed several times using absolute ethanol,
166 and dried under vacuum at 50 °C (Figure 1).



167

168 **Figure 1.** Scheme of $\text{Fe}_3\text{O}_4@\text{SiO}_2\text{-N}_n$ nanoparticles synthesis.

169

170 2.5. Methods

171 The images of all $\text{Fe}_3\text{O}_4@\text{SiO}_2\text{-N}_n$ nanoparticles were obtained using the scanning
172 electron microscope (SEM) — JEOL JSM7001F, operating at 9.5 kV — and transmission
173 electron microscopy (TEM) — Tecnai G2 Spirit BioTWIN FEI, operating at 120 kV. All
174 nanoparticles samples for TEM imaging were sonicated for 30 min in the absolute ethanol
175 solution.

176 Fourier Transform Infrared Spectroscopy (FT-IR) spectra were obtained with the KBr
177 pellet method using Bruker FRA 106 spectrometer.

178 X-Ray Photoelectron Spectroscopy (XPS) was utilised to evaluate the chemical
179 composition of the investigated nanoparticles. For this purpose, the high-resolution scans were
180 performed in Fe2p, C1s, O1s, N1s, and Si2p binding energy range. The measurements were
181 carried out on Escalab 250Xi spectroscope, ThermoFisher Scientific. The monochromatic $\text{AlK}\alpha$
182 excitation source was used with a spot diameter of 250 μm . 10 eV pass energy and 0.05 eV
183 energy step size were utilised. The charge compensation was achieved through the low-energy
184 electron and low-energy Ar^+ ions flow, with the final calibration of the XPS spectra for peak
185 characteristics adventitious carbon C1s at 284.7 eV. The peak deconvolution was carried out
186 using Avantage software provided by the spectroscope manufacturer.

187 All electrochemical measurements were carried out using Mercury Electrode Metrohm
188 663 VA Stand integrated with Autolab potentiostat/galvanostat PGSTAT-128N controlled with
189 NOVA 2.1.4 software. The three-electrode cell contained Static Drop Mercury Electrode
190 (SDME) as a working electrode. Calomel $\text{Hg}|\text{Hg}_2\text{Cl}_2|\text{KCl}_{(\text{saturated})}$ and glassy carbon (GC) were
191 used as the reference and counter electrode, respectively.

192 Differential pulse voltammetry (DPV) was utilised for the detection of Cd^{2+} , Pb^{2+} , and
193 Cd^{2+} ions under optimised experimental conditions: deposition potential -0.9 V, deposition time
194 90 s, modulation amplitude 0.05 V, modulation time 0.07 s, interval time 1.85 s, and step
195 potential 0.005 V. All measurements were conducted in Teflon cell to avoid a sorption of metal
196 ions on the glass surface.

197 The ion detection was performed in a potential range of -0.8 V to 0.0 V. The solutions
198 of metal ions were prepared using potassium chloride KCl, pH 6.5 as the supporting electrolyte.
199 $\text{Fe}_3\text{O}_4@\text{SiO}_2\text{-N}_n$ nanoparticles were prepared by dispersion using the ultrasonic bath for 30 min
200 before each measurement.

201
202
203

204 **2.6. Determination of removal efficiency**

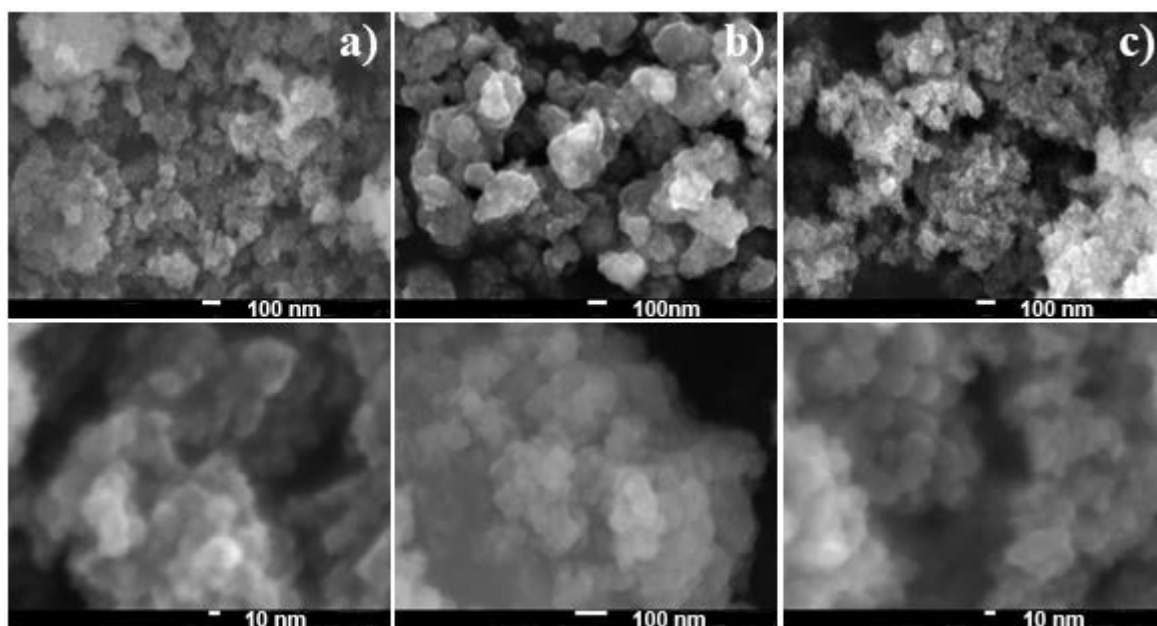
205 The adsorption-desorption experiment was conducted to examine the efficiency of Cu^{2+}
206 removal from an aqueous solution. The ion desorption process was investigated in 0.1 M HCl
207 solution which was used as a desorbing agent. 5.08 mg of $\text{Fe}_3\text{O}_4@\text{SiO}_2\text{-N}_3$ was used to capture
208 copper ions present in 10 mL of 4.3 μM Cu^{2+} solution. The solution was then left for 40 min at
209 room temperature with shaking. Subsequently, all nanoparticles were collected magnetically
210 and the supernatant was removed. Then, 10 mL of 0.1 M HCl was added to $\text{Fe}_3\text{O}_4@\text{SiO}_2\text{-N}_3$
211 nanoparticles with adsorbed Cu^{2+} and mixed with a stream of argon. The measurement of
212 desorbed Cu^{2+} concentration was performed immediately using DPASV technique. The removal
213 efficiency was calculated by the determination of the obtained voltammograms peak area for
214 the standard solution and after desorption in 0.1 M HCl.

215

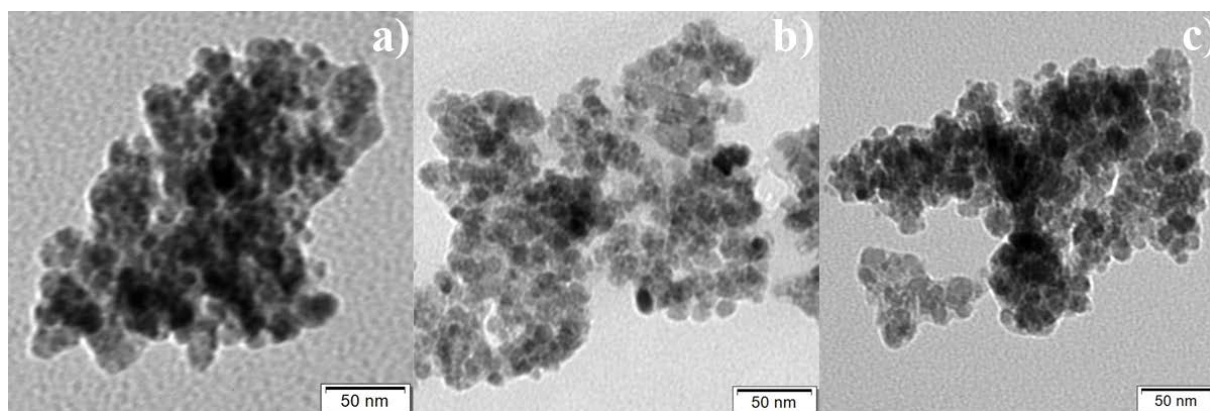
216 **3. Results and discussion**

217 **3.1. SEM and TEM — Morphology analysis**

218 In the first step, the obtained $\text{Fe}_3\text{O}_4@\text{SiO}_2\text{-N}_n$ nanoparticles were characterised using
219 Scanning Electron Microscopy and Transmission Electron Microscopy (Figure 2). SEM and
220 TEM images of magnetite nanoparticles modified with different length of amino chains showed
221 that the nanostructures received by co-precipitation method are highly homogeneous in shape
222 and size. Figure 3 confirms the presence of small and quasi-spherical core-shell structures. The
223 average size of all $\text{Fe}_3\text{O}_4@\text{SiO}_2\text{-N}_n$ nanoparticles was approximately 30 – 50 nm. All of the
224 examined nanoparticles were in the agglomerated state due to their natural tendency to form
225 agglomerates based on their magnetic nature.



226 **Figure 2.** SEM images of: column a) $\text{Fe}_3\text{O}_4@\text{SiO}_2\text{-N}_1$, column b) $\text{Fe}_3\text{O}_4@\text{SiO}_2\text{-N}_2$,
227 and column c) $\text{Fe}_3\text{O}_4@\text{SiO}_2\text{-N}_3$.
228



229 **Figure 3.** TEM images of: a) $\text{Fe}_3\text{O}_4@\text{SiO}_2\text{-N}_1$, b) $\text{Fe}_3\text{O}_4@\text{SiO}_2\text{-N}_2$, and c) $\text{Fe}_3\text{O}_4@\text{SiO}_2\text{-N}_3$.
230
231

3.2. FT-IR spectroscopy analysis

The FT-IR spectra were obtained to compare the spectroscopic differences and to validate the presence of functional groups on the nanomagnetite surface. Figure 4 a) shows the FT-IR spectra for pure Fe_3O_4 nanoparticles and silica-coated $\text{Fe}_3\text{O}_4@ \text{SiO}_2$ as a reference and for nanoparticles functionalised by amino groups $\text{Fe}_3\text{O}_4@ \text{SiO}_2\text{-N}_1$, $\text{Fe}_3\text{O}_4@ \text{SiO}_2\text{-N}_2$, and $\text{Fe}_3\text{O}_4@ \text{SiO}_2\text{-N}_3$. For all samples, two characteristic bands were shown at wavenumbers 453 cm^{-1} and 597 cm^{-1} from metal-oxygen stretching at Fe^{3+} site [56–58]. In all IR spectra, the decrease in the intensity of the Fe-O band for nanoparticles coated with silica and amino groups was observed. The decrease in the band intensity confirms that the nanoparticles surface was successfully functionalised [59]. Spectra for silica-coated nanoparticles showed a broad, strong band near 1096 cm^{-1} region assigned to symmetric and asymmetric Si-O-Si stretching vibrations caused by the coating of silica shells on the magnetite surface [60].

On the spectra of all amino-modified nanoparticles (Figure 4 b) a new band appeared in the region of 1563 cm^{-1} and 3402 cm^{-1} attributed to N-H stretching vibrations of amino groups. These bands confirm the successful amino-functionalisation of the silica layer on $\text{Fe}_3\text{O}_4@ \text{SiO}_2$ nanoparticles and the presence of terminal $-\text{NH}_2$ [61,62].

Additionally, a weak band at 1458 cm^{-1} attributed to the C-N stretch vibration was noticed [63]. The absorption bands at about 2930 cm^{-1} and 2850 cm^{-1} are the result of C-H stretching vibrations in the carbon chain [64].

These FT-IR spectra confirmed the formation of a silica shell on the surface of Fe_3O_4 and the amino-functionalisation of the $\text{Fe}_3\text{O}_4@ \text{SiO}_2$ core-shell nanostructures.

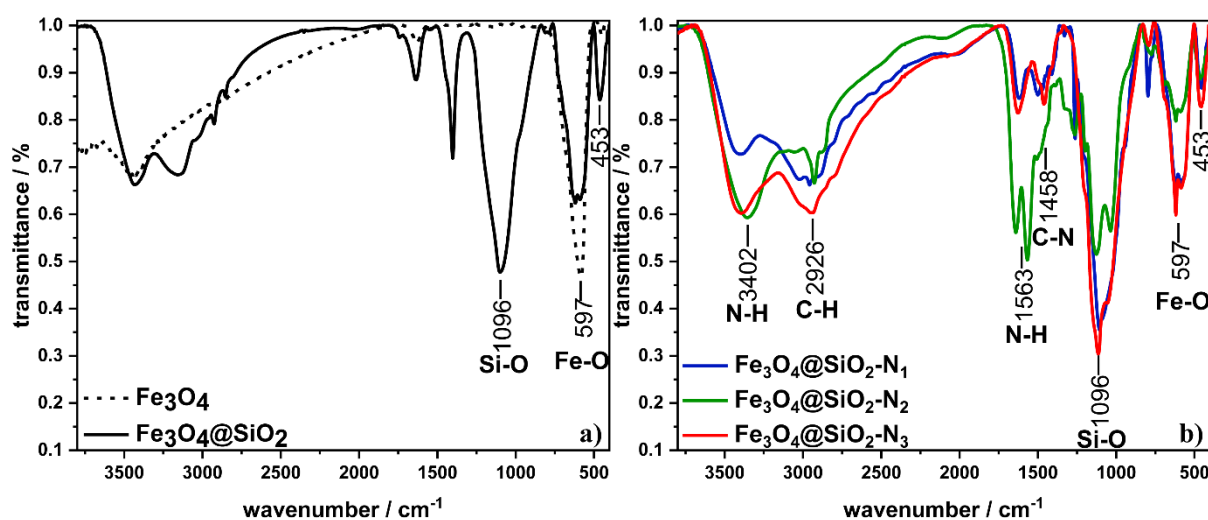
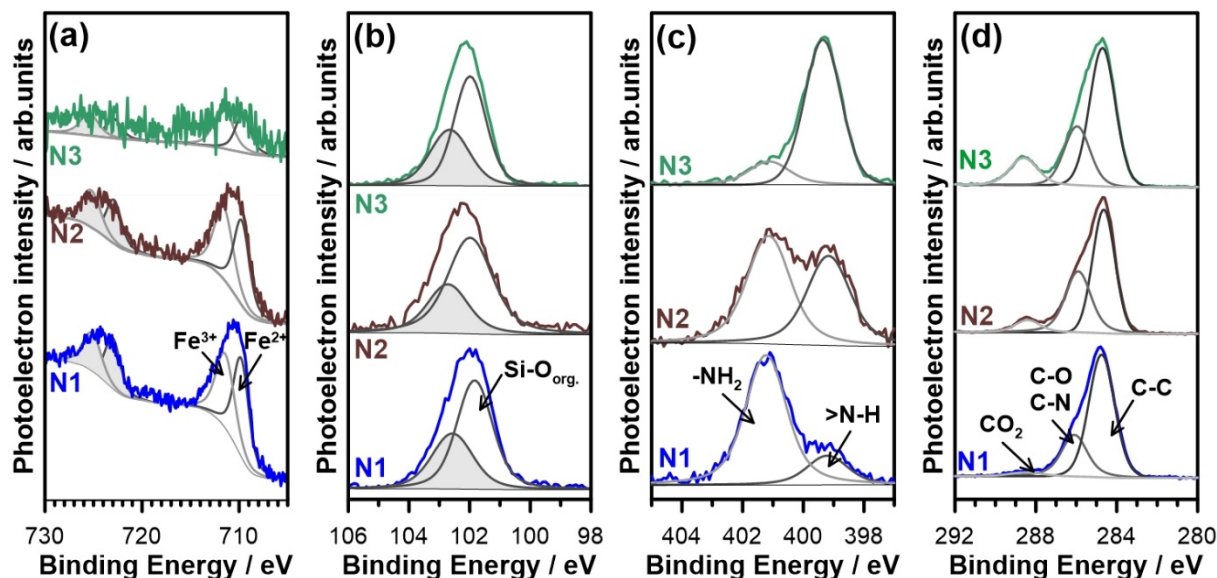


Figure 4. FT-IR spectra for non-functionalised a) Fe_3O_4 , $\text{Fe}_3\text{O}_4@ \text{SiO}_2$ and b) functionalised $\text{Fe}_3\text{O}_4@ \text{SiO}_2\text{-N}_1$, $\text{Fe}_3\text{O}_4@ \text{SiO}_2\text{-N}_2$, and $\text{Fe}_3\text{O}_4@ \text{SiO}_2\text{-N}_3$ nanoparticles.

257 3.3. XPS analysis

258 Moreover, we performed the XPS analyses for all obtained samples to confirm the
 259 structure of formed core-shell nanoparticles. The results of the high-resolution XPS analysis
 260 are collectively presented in Figure 5 and Table 1 for each of the analysed samples.



261 Figure 5. High-resolution XPS spectra obtained for each investigated nanoparticle
 262 $\text{Fe}_3\text{O}_4@\text{SiO}_2\text{-N}_1$, $\text{Fe}_3\text{O}_4@\text{SiO}_2\text{-N}_2$, and $\text{Fe}_3\text{O}_4@\text{SiO}_2\text{-N}_3$ within the analysed binding energy
 263 range: (a) $\text{Fe}2p$, (b) $\text{Si}2p$, (c) $\text{N}1s$, and (d) $\text{C}1s$ with superimposed deconvolution according to
 264 the model described below. The grey areas represent the $\text{Fe}2p_{1/2}$ and $\text{Si}2p_{1/2}$ peaks in $\text{Fe}2p$ and
 265 $\text{Si}2p$ peak doublets, respectively.
 266

267
 268 The deconvolution in $\text{Fe}2p$ binding energy (BE) range can be carried out with two spin-
 269 orbit doublets, characteristic for both Fe^{2+} and Fe^{3+} . Furthermore, $\text{Fe}2p$ signal for $\text{Fe}_3\text{O}_4@\text{SiO}_2\text{-N}_3$
 270 was barely detected [65–67]. The peak position remains unaltered for each studied
 271 compound, proving that modification of the organic chain does not influence the inner shell
 272 structure. Similar to the case of Fe_3O_4 , the amount of silica is at its peak for $\text{Fe}_3\text{O}_4@\text{SiO}_2\text{-N}_1$
 273 functionalisation. Moreover, the significant differences were not observed between
 274 $\text{Fe}_3\text{O}_4@\text{SiO}_2\text{-N}_2$ and $\text{Fe}_3\text{O}_4@\text{SiO}_2\text{-N}_3$ samples in this case, what may imply that the thickness
 275 of the organic amino shell is similar for both of these nanoparticles.

276 The shape of recorded $\text{N}1s$ spectra reveal major differences between the analysed
 277 samples. Each of the nanoparticles contains nitrogen in two different chemical states, while
 278 their quantity differs significantly. Two deconvolution spectra used in the proposed model peak
 279 at 399.2 and 401.2 eV. The peak at higher BE's, dominant in the case of $\text{Fe}_3\text{O}_4@\text{SiO}_2\text{-N}_1$
 280 sample, should represent the terminal amino- NH_2 functional groups in the compound. The

281 presence of >N-H tertiary amino groups in Fe₃O₄@SiO₂-N₂ and Fe₃O₄@SiO₂-N₃ nanoparticles
282 is reflected in *N1s* spectra with the increasing contribution of the component, located at lower
283 binding energy range. Here, the share of terminal amino groups is reduced to 45 % for
284 Fe₃O₄@SiO₂-N₂ and to 18 % for Fe₃O₄@SiO₂-N₃ samples. The aforementioned model finds a
285 good correlation with the literature findings. The presence of N-H groups in Fe₃O₄@SiO₂-N₁
286 can be associated with the adsorption of CO₂ from the ambient atmosphere [68–70].

287 The presence of Si-O bonds with the organic chain was confirmed by a strong peak
288 doublet at 101.7 eV. Similar values were previously reported for silicone groups in silanes and
289 other organic, silicon-containing compounds [58,71]. Finally, the *C1s* peak region was analysed
290 and deconvoluted in three different chemical states. The most significant component, detected
291 at 284.7 eV, should be ascribed to C-C and C-H bonds in the functionalisation molecules
292 forming the shell of the nanoparticles. Its total share in the analysed signal ranges between 33.3
293 and 36.8 at.%. Importantly, the presence of the component mentioned above may be caused by
294 adventitious carbon from the air exposure [72]. The second notable component lies at 286.2 eV,
295 an energy range typical for C-N bonds in amines and C-O bonds [73,74]. The share of the
296 organic chain (measured as a sum of C-C and C-N components) is naturally the most prominent
297 for the shortest amino chains with Fe₃O₄@SiO₂-N₁ molecule functionalisation. However, the
298 significant differences were not observed between Fe₃O₄@SiO₂-N₂ and Fe₃O₄@SiO₂-N₃
299 samples, what is similar to the earlier conclusion regarding *Si2p* component. Finally, the last
300 *C1s* peak emerges for both Fe₃O₄@SiO₂-N₂ and Fe₃O₄@SiO₂-N₃ samples, at energies
301 exceeding 288 eV. This component is most often ascribed to carbon dioxide, which is probably
302 adsorbed onto the nanoparticles surface [75]. Surface defects as well as structure modifications
303 of the examined compounds influence the CO₂ adsorption [76,77]. Since its contribution is the
304 highest for the Fe₃O₄@SiO₂-N₃ sample, it is suggested that its presence is connected with
305 changes within >NH groups.

306 These analyses are confirmed in the distribution of various components in *O1s* spectra,
307 which were deconvoluted in three peaks, connected with iron oxides (529.9 eV), silica, and
308 possible C-O interaction (531.7 eV) and C=O bonds (533.5 eV). The Fe₃O₄ signal is the
309 strongest for Fe₃O₄@SiO₂-N₁ sample and is up to four times weaker for Fe₃O₄@SiO₂-N₃,
310 where, on the other hand, the signal from C=O bonds is more prominent. The two times higher
311 contribution from silica in the *O1s* of Fe₃O₄@SiO₂-N₁ sample was also confirmed, strongly
312 supporting the hypothesis regarding the smaller functionalisation thickness of these
313 nanoparticles.

314

315 **Table 1.** Surface chemical composition of Fe₃O₄@SiO₂-N₁, Fe₃O₄@SiO₂-N₂, and
 316 Fe₃O₄@SiO₂-N₃ samples based on the deconvoluted high-resolution XPS spectra.

BE / eV	<i>Fe2p</i>		<i>Si2p</i>	<i>N1s</i>		<i>C1s</i>			<i>O1s</i>		
	Fe ²⁺	Fe ³⁺	Si-O	>NH	-NH ₂	C-C	CN	C=O	Fe-O	Si-O	C=O
	709.8	711.4	101.7	399.2	401.2	284.7	286.1	288.5	529.9	531.7	533.5
N ₁	1.1	1.0	13.0	1.3	5.7	33.3	12.8	1.3	4.0	25.3	1.2
N ₂	0.7	0.7	7.9	2.8	3.4	34.2	22.0	4.4	2.6	16.9	4.3
N ₃	0.1	0.1	7.9	8.2	1.7	36.8	16.1	8.0	0.9	17.0	3.1

317

318

3.4. Simultaneous electrochemical determination of Cd²⁺, Pb²⁺, and Cu²⁺

The individual and simultaneous determination of Cd²⁺, Cu²⁺, and Pb²⁺ applying amino-functionalised Fe₃O₄@Carbon microspheres were previously measured by Bai et al. [78] using modified glassy carbon electrode.

In this work, the simultaneous detection of Cd²⁺, Pb²⁺, and Cu²⁺ was carried out under optimised experimental conditions using DPASV technique and HDM electrode. The main advantage of these electrodes, besides its surface reproducibility and fast measurement, [79] is the analysis of Fe₃O₄@SiO₂-N_n nanoparticles to assess their capability for binding the metal ions without electrode modification. We investigated three types of nanoparticles differing in the number of amino groups in the outer carbon chain — Fe₃O₄@SiO₂-N₁ with one amino group, Fe₃O₄@SiO₂-N₂ with two amino groups, and Fe₃O₄@SiO₂-N₃ with three amino groups.

To achieve this goal, all measurements were conducted under laboratory conditions to reduce the risk of environmental mercury contamination. Mercury from HDME can be reused after proper treatment. Two-stage DPASV analysis involved pre-concentration and metal ions stripping. First, the Cd²⁺, Pb²⁺, and Cu²⁺ ions were electrodeposited onto the working electrode by application of the negative potential (-0.9 V). Subsequently, the faradic current obtained by oxidation was recorded during the potential sweep toward the anodic direction (-0.8 V to 0.0 V).

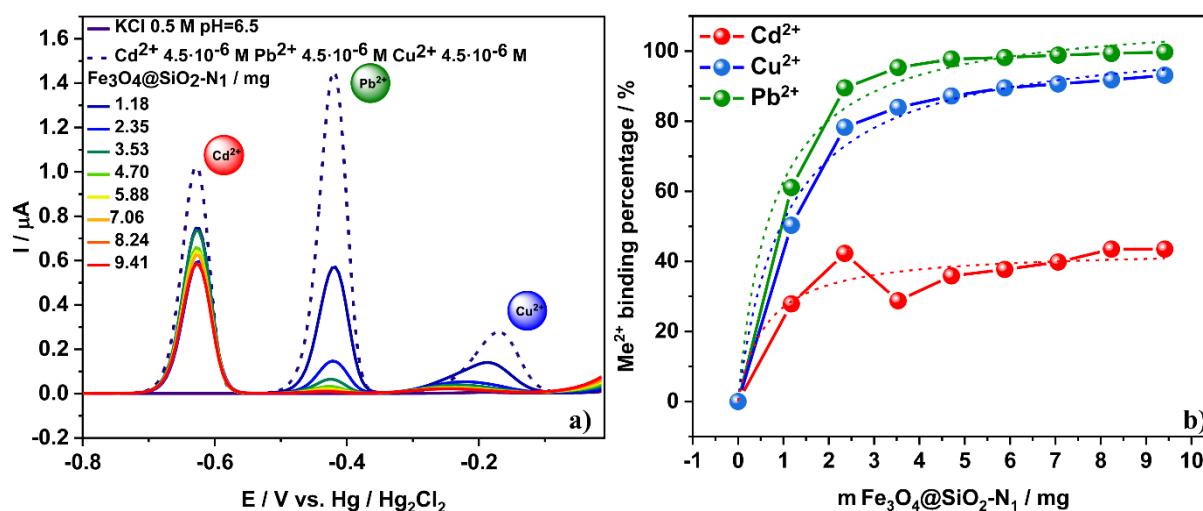
To examine the selected ion binding abilities of Fe₃O₄@SiO₂-N₁, Fe₃O₄@SiO₂-N₂, and Fe₃O₄@SiO₂-N₃, series of measurements were performed in the solution containing Cd²⁺, Pb²⁺, and Cu²⁺, 4.5 μM concentration. All electrochemical experiments were performed in 0.5 M KCl pH = 6.5 due to the formation of hydroxides of utilised metals at pH higher than 7 [58]. Furthermore, the adsorption of metal ions depends on the charge located on the nanocomposite surface and the number of functional groups [80].

Three well-defined peaks at -0.63 V, -0.42 V, and -0.17 V in anodic stripping voltammograms confirm the presence of Cd²⁺, Pb²⁺, and Cu²⁺ in the solution, respectively (see, Figure 6). During the next portions of nanoparticles addition, a decrease in the intensity of the ions peaks was observed. The rate of peaks intensity change depended on the determined ion and used nanoparticles type. In all presented voltammograms, the dilution factor was expressed by the formula: $DF = \frac{V_0 + V_s}{V_0}$, where V₀ is the initial volume and V_s is the step volume applied.

Figure 6 a) presents the voltammograms obtained during the titration of Cd²⁺, Pb²⁺, and Cu²⁺ by Fe₃O₄@SiO₂-N₁. The metal ion peaks intensity decreased during the addition of the next portions of nanoparticles in an amount of 1.18 mg to 9.41 mg, conducted in eight steps.

351 The obtained results directly indicate that the initial linear current peak (blue intermittent line)
 352 decreases for Pb^{2+} and Cu^{2+} ions of each nanoparticles portion.

353 The intensity of Cd^{2+} peak decreased by a half and remained at this stable level. After
 354 the addition of 7.06 mg of nanoparticles, the equilibrium was established and the next portion
 355 of nanoparticles caused no changes in the current peak intensity. The $\text{Fe}_3\text{O}_4@\text{SiO}_2\text{-N}_1$ binding
 356 percentage was calculated (Figure 6 b) for Pb^{2+} and Cu^{2+} and reached 99.7 % and 92.8 %,
 357 respectively. However, the binding percentage for Cd^{2+} remained stable at the level of 40 %.
 358 These results indicate that $\text{Fe}_3\text{O}_4@\text{SiO}_2\text{-N}_1$ nanoparticles express high sensitivity towards Pb^{2+}
 359 and Cu^{2+} , what is observed by binding of these ions in nearly 100 %.



360
 361 **Figure 6.** a) Anodic stripping voltammograms and b) percentage of Cd^{2+} (4.5 μM),
 362 Pb^{2+} (4.5 μM) and Cu^{2+} (4.5 μM) binding by $\text{Fe}_3\text{O}_4@\text{SiO}_2\text{-N}_1$ nanoparticles.

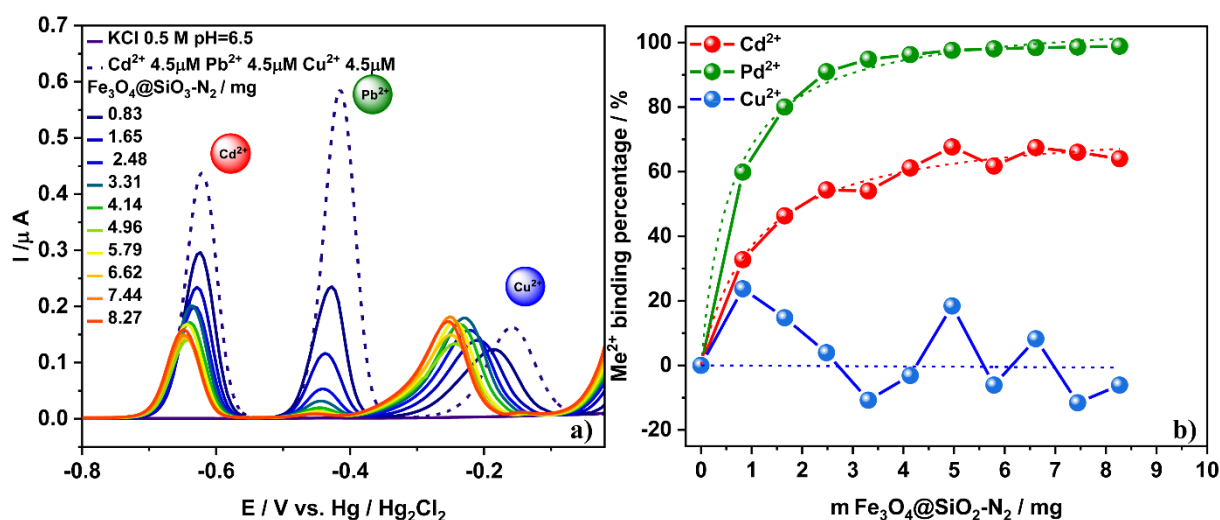
363
 364 In the next step, we conducted the simultaneous experiments using Cd^{2+} , Pb^{2+} and Cu^{2+}
 365 to evaluate the $\text{Fe}_3\text{O}_4@\text{SiO}_2\text{-N}_2$ nanoparticles binding capacity. The titration of Cd^{2+} , Pb^{2+} , and
 366 Cu^{2+} was carried out in five steps using various amounts of $\text{Fe}_3\text{O}_4@\text{SiO}_2\text{-N}_2$ nanoparticles —
 367 0.83 mg to 8.27 mg (Figure 7a).

368 Surprisingly, besides a decrease in the peak intensity observed during Cd^{2+} , Pb^{2+}
 369 titration, we also detected a slight shift in the peaks towards lower potentials. Figure 7a shows
 370 the voltammograms where a complete disappearance of Pb^{2+} peak and decrease in the Cd^{2+}
 371 peak intensity were observed.

372 In the case of Cu^{2+} titration (Figure 7a), the effect of the signal decreasing is observed
 373 only in the first two steps, following a comparable signal level afterwards, shifted toward
 374 negative potentials. This phenomenon is probably associated with the adsorption of

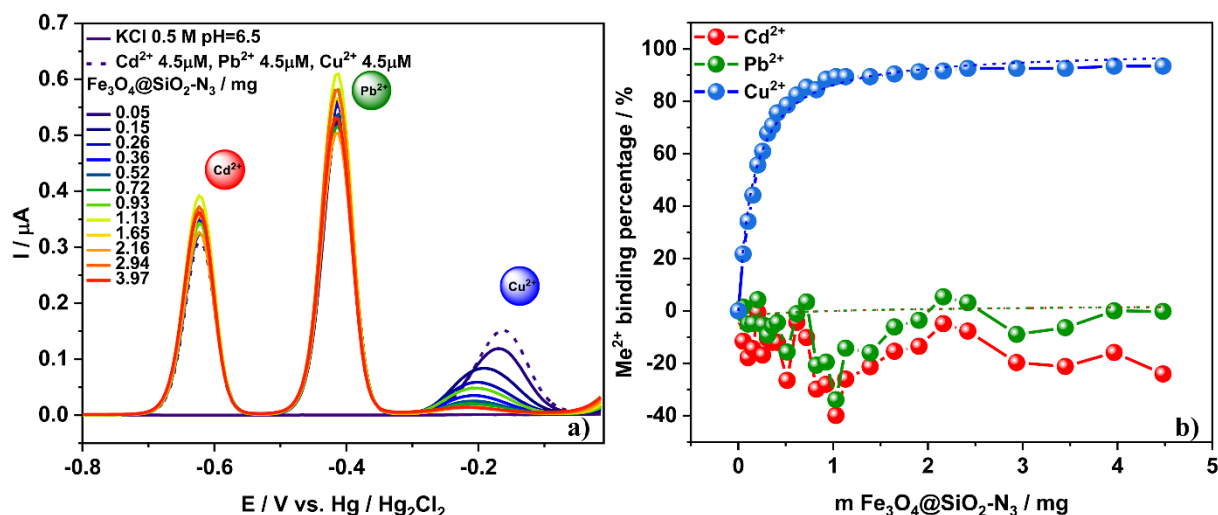
375 nanoparticles and their complexes to the mercury drop [81]. The irregular changes in the peak
 376 intensity clearly indicate that the equilibrium is not establishing.

377 After addition of 3.31 mg $\text{Fe}_3\text{O}_4@\text{SiO}_2\text{-N}_2$ no significant changes in the voltammogram
 378 were observed. Figure 7b shows the binding percentage for $\text{Fe}_3\text{O}_4@\text{SiO}_2\text{-N}_2$ nanoparticles. The
 379 percentage of Pb^{2+} and Cd^{2+} ion binding by $\text{Fe}_3\text{O}_4@\text{SiO}_2\text{-N}_2$ was established at 98.5 % and
 380 66.6%, respectively. It is worth to notice that there was no ion binding observed for Cu^{2+} . The
 381 percentage of Cu^{2+} binding by $\text{Fe}_3\text{O}_4@\text{SiO}_2\text{-N}_2$ remains at 0 % even if nanoparticles were added
 382 in an excess. An average of obtained results and slight differences in Cu^{2+} peak intensity were
 383 regarded as measurement errors.



384
 385 **Figure 7.** a) Anodic stripping voltammograms and b) percentage of Cd^{2+} (4.5 μM),
 386 Pb^{2+} (4.5 μM), and Cu^{2+} (4.5 μM) binding by $\text{Fe}_3\text{O}_4@\text{SiO}_2\text{-N}_2$ nanoparticles.

387
 388 The voltammograms presented in Figure 8a reveal the Cd^{2+} , Pb^{2+} , and Cu^{2+} titration by
 389 $\text{Fe}_3\text{O}_4@\text{SiO}_2\text{-N}_3$ in twelve steps in the nanoparticles amount range of 0.05 mg to 3.97 mg. The
 390 addition of the next nanoparticles portions led only to the disappearance of the Cu^{2+} peak. The
 391 Cd^{2+} and Pb^{2+} slight peak intensity changes were considered to be in the range of measurement
 392 error. For $\text{Fe}_3\text{O}_4@\text{SiO}_2\text{-N}_3$ nanoparticles, the Cu^{2+} binding percentage reached 92.5 %, while
 393 0 % binding percentage was observed for Cd^{2+} and Pb^{2+} ions (Figure 8 b).

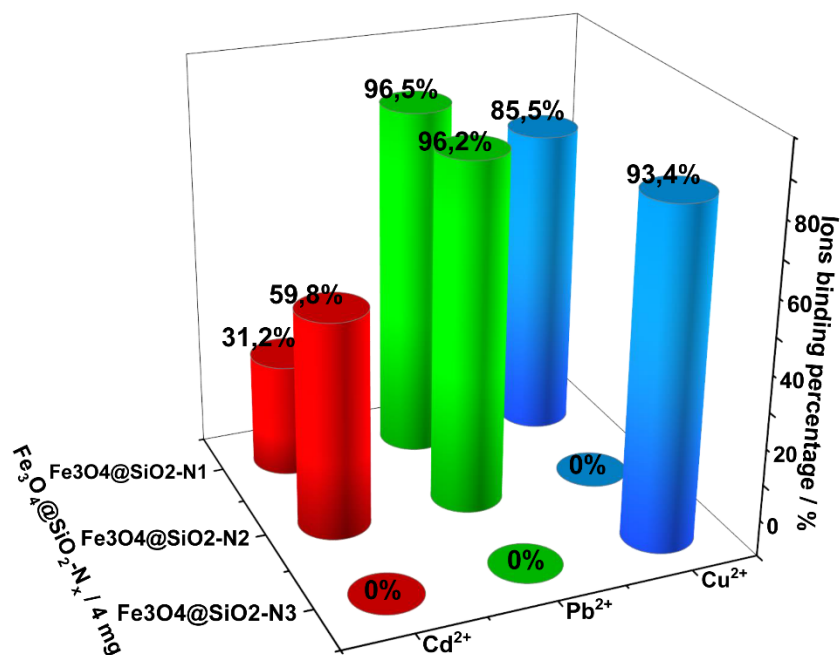


394
 395 **Figure 8.** a) Anodic stripping voltammograms and b) percentage of Cd^{2+} (4.5 μM),
 396 Pb^{2+} (4.5 μM), and Cu^{2+} (4.5 μM) binding by $\text{Fe}_3\text{O}_4@\text{SiO}_2\text{-N}_3$ nanoparticles.

397
 398 Figure 9 presents the comparison of ion binding percentage for each $\text{Fe}_3\text{O}_4@\text{SiO}_2\text{-N}_n$
 399 nanoparticle. The binding percentage was recounted for 4 mg of nanoparticles added to the ion
 400 solution. The highest observed binding percentage for Pb^{2+} was over 96%, both for
 401 $\text{Fe}_3\text{O}_4@\text{SiO}_2\text{-N}_1$ and $\text{Fe}_3\text{O}_4@\text{SiO}_2\text{-N}_2$. The slightly smaller binding percentage was observed
 402 for Cu^{2+} binding by $\text{Fe}_3\text{O}_4@\text{SiO}_2\text{-N}_3$ and $\text{Fe}_3\text{O}_4@\text{SiO}_2\text{-N}_1$ resulting in 93.4 % and 85.5 %,
 403 respectively.

404 Furthermore, there was no Cd^{2+} , Pb^{2+} , and Cu^{2+} binding observed for $\text{Fe}_3\text{O}_4@\text{SiO}_2\text{-N}_3$,
 405 $\text{Fe}_3\text{O}_4@\text{SiO}_2\text{-N}_3$, and $\text{Fe}_3\text{O}_4@\text{SiO}_2\text{-N}_2$, respectively. These results directly indicate that the
 406 $\text{Fe}_3\text{O}_4@\text{SiO}_2\text{-N}_3$ nanoparticles bind Cu^{2+} with high selectivity.

407
 408



409
410
411
412
413

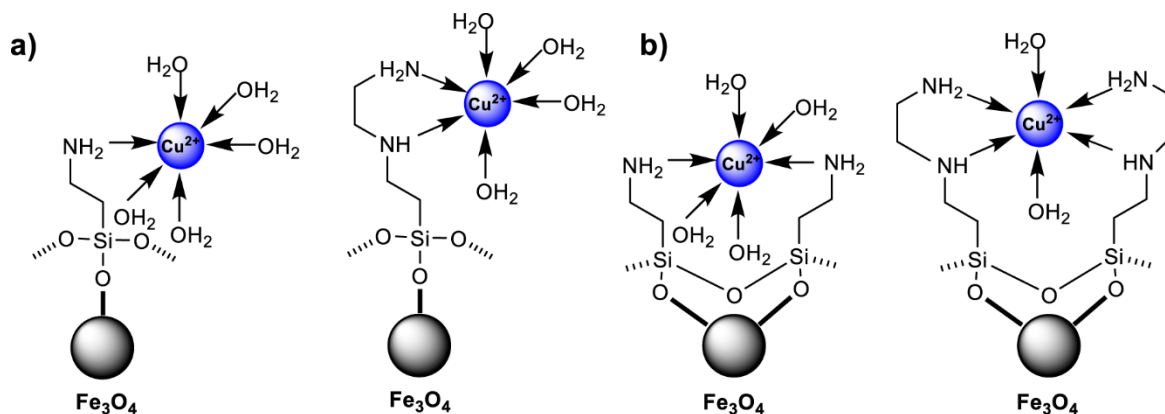
Figure 9. Cd²⁺, Pb²⁺, Cu²⁺ ions binding percentage for Fe₃O₄@SiO₂-N₁, Fe₃O₄@SiO₂-N₂ and Fe₃O₄@SiO₂-N₃ nanoparticles

414 On the basis of the structural characteristics of Cu (II) diamine complexes supported on
415 silica gel and the distribution of these forms as a function of the pH solution described by
416 Nowicki [82], the proposed structure of copper complex formation by Fe₃O₄@SiO₂-N_n is pre-
417 sented in Figure 10. It seems that formation of complexes with metal ions with 1:1 and 1:2
418 stoichiometry is the key factor in the complexation of ions by amines in the hybrid material
419 (Figure 10).

420 The number of donor nitrogen atoms in the structure of the complexes, the size of the
421 ions, the density of the charge of metal ions, and the number of water molecules that hydrate
422 both the complexes and ligands significantly determine the stoichiometry and the process of
423 complex formation by the hybrid material [83].

424 The differences in the binding selectivity for the examined metal ions by
425 Fe₃O₄@SiO₂-N_n is probably related to the presence of intramolecular hydrogen bonds occurring
426 both in the external and internal parts of the functional layer. The observation that
427 Fe₃O₄@SiO₂-N₁ binds Cd²⁺, Pb²⁺, Cu²⁺, Fe₃O₄@SiO₂-N₂ binds Cd²⁺, Pb²⁺, and
428 Fe₃O₄@SiO₂-N₃ binds only Cu²⁺ results from these interactions. The aqua and amino com-
429 plexes form between metal ions and amines with the deposition directly on a hybrid material.
430 Subsequently, free electron pairs in this material, which come to varying degrees from nitrogen

431 atoms of amines, determine the manner and selectivity of the ion binding with the studied ma-
432 terial.



433
434 **Figure 10.** Proposed structure of the two-type complexes a) 1:1 and b) 1:2 $\text{Fe}_3\text{O}_4@ \text{SiO}_2\text{-N}_n$
435 nanoparticles and ion metal interactions.

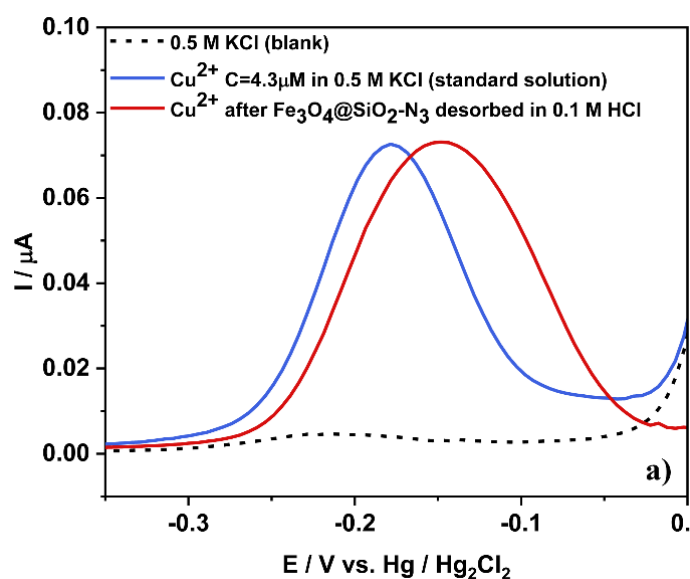
436

437 3.5. Cu^{2+} adsorption-desorption experiment using $\text{Fe}_3\text{O}_4@\text{SiO}_2\text{-N}_3$ nanoparticles

438

439 Based on the high selectivity of $\text{Fe}_3\text{O}_4@\text{SiO}_2\text{-N}_3$ for Cu^{2+} which was observed using
440 electrochemical method, we decided to evaluate the adsorption-desorption properties only of
441 this studied nanoparticle. It is worth to notice that, according to the authors' knowledge, this
442 experiment using DPASV was performed for the first time. The procedure of Cu^{2+} adsorption
443 was described in the experimental section. 5.08 mg of $\text{Fe}_3\text{O}_4@\text{SiO}_2\text{-N}_3$ was used to bind
444 43 nmol of Cu^{2+} in 0.5 M KCl solution. The adsorption process for nanoparticles containing an
445 amino group is usually performed from a couple of minutes to hours [84–86,43]. In this work,
446 the adsorption process was performed within 40 min incubation time at room temperature, with
447 shaking. The desorption process was performed in 0.1 M HCl to obtain acidic pH and
448 protonation of amino groups leading to the Cu^{2+} ions desorption. The desorption process was
449 conducted using DPASV method directly after the addition of HCl. According to the previous
450 research, the hydrochloric acid was selected as an optimal desorption agent [61,84]. In other
451 study the desorption time ranged from 5 min to 40 min [43,85]. We, however, established the
452 desorption time which was shorter than 5 minutes. Figure 11 shows the voltammograms
453 obtained for standard Cu^{2+} solution and after the nanoparticles regeneration. The peak shift is
454 the consequence of different pH of the solution. The calculated Cu^{2+} removal efficiency was
455 99.9 %.

456



457

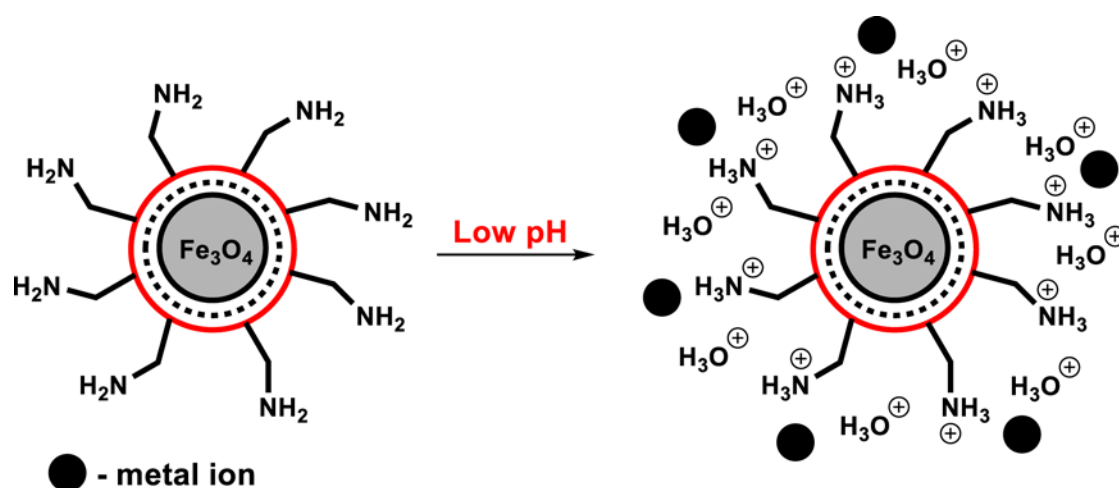
458 **Figure 11.** Comparison of anodic stripping voltammograms of 0.5 M KCl electrolyte (blank),

459 Cu^{2+} standard solution $C = 4.3 \mu\text{M}$, Cu^{2+} after $\text{Fe}_3\text{O}_4@\text{SiO}_2\text{-N}_3$ nanoparticles regeneration.

460

461 Proper selection of pH range, which effects the behaviour of the nanoparticles, the form
 462 of determined metal ion, and its solubility, is the most important factor for the examination of
 463 the adsorption and desorption process efficiency [86]. The form of Cu^{2+} depends on the pH
 464 value of the solution. Cu^{2+} species occur at $\text{pH} < 7$ [84,87]. At $\text{pH} > 7$ different derivative
 465 products of Cu^{2+} hydrolysis — $\text{Cu}_2(\text{OH})_2^{2+}$, $\text{Cu}(\text{OH})^+$, $\text{Cu}(\text{OH})_2$, $\text{Cu}(\text{OH})_3^-$, $\text{Cu}(\text{OH})_4^-$ — exist
 466 in the solution [88]. The Cu^{2+} quantity drops with the increasing pH value, what leads to the
 467 precipitation of various hydrolysis forms of Cu^{2+} . Due to this phenomenon, the adsorption
 468 process was performed at pH 6.5.

469 The adsorption and desorption process occurring for the studied nanoparticles is the
 470 consequence of the acid-base interactions. In an aqueous solution both H_3O^+ and metal ions
 471 undergo the adsorption processes onto amino groups present in $\text{Fe}_3\text{O}_4@\text{SiO}_2\text{-N}_n$ nanoparticles
 472 (Figure 12). Low pH value causes the increase of H_3O^+ species in a solution and the protonation
 473 of amino groups present on the nanoparticles surface. This, in consequence, leads to the
 474 decrease in the metal ion concentration due to the nanoparticle adsorption (Figure 12). On the
 475 other hand, high pH value is associated with the elevated number of hydroxyl groups in the
 476 solution, what causes the amino groups deprotonation (Figure 12). In consequence, the
 477 deprotonated amino groups increased the capability of the nanoparticles to bind metal ions [86].
 478



480 **Figure 12.** Scheme of the proposed adsorption and desorption mechanism for
 481 the $\text{Fe}_3\text{O}_4@\text{SiO}_2\text{-N}_n$ nanoparticles — metal ions interaction.
 482

483 4. Conclusions

484 In present work we examined a series of functionalised magnetite nanoparticles
485 $\text{Fe}_3\text{O}_4@\text{SiO}_2\text{-N}_n$ as a novel Cd^{2+} , Pb^{2+} , Cu^{2+} nano-adsorbent in KCl aqueous solution.

486 First, we synthesised the nanoparticles coated preliminary with SiO_2 using TEOS and
487 then with various carbon chains containing a different number of amino groups —
488 $\text{Fe}_3\text{O}_4@\text{SiO}_2\text{-N}_1$, $\text{Fe}_3\text{O}_4@\text{SiO}_2\text{-N}_2$, and $\text{Fe}_3\text{O}_4@\text{SiO}_2\text{-N}_3$. FT-IR and XPS spectra confirmed the
489 presence of characteristic functional groups on the nanoparticles surface. Additionally, SEM
490 and TEM analysis were utilised to confirm the homogenous spherical 30 to 50 nm
491 nanostructures.

492 These three types of obtained nanoparticles were used as Cd^{2+} , Pb^{2+} , Cu^{2+} metal ion
493 adsorbents. Metal ion binding ability of $\text{Fe}_3\text{O}_4@\text{SiO}_2\text{-N}_n$ was measured using DPASV method
494 in combination with HDME in 0.5 M KCl solution.

495 To compare binding capacity in 4.5 μM Cd^{2+} , Pb^{2+} , and Cu^{2+} solutions, the binding
496 percentage was recalculated for 4 mg of used nanoparticles. Obtained results show that the
497 adsorption rate is different for each ion depending on the nanoparticles type. The ion binding
498 capacity and selectivity depends on the interactions occurring between the outer carbon amino
499 chains and the metal ion.

500 The highest binding percentage — 96 % — was observed for Pb^{2+} binding for both
501 $\text{Fe}_3\text{O}_4@\text{SiO}_2\text{-N}_1$ and $\text{Fe}_3\text{O}_4@\text{SiO}_2\text{-N}_2$. Furthermore, slightly lower binding level of nearly 93 %
502 was observed for $\text{Fe}_3\text{O}_4@\text{SiO}_2\text{-N}_3$ Cu^{2+} . The middle value of the binding percentage — 85% —
503 was observed for Cu^{2+} binding by $\text{Fe}_3\text{O}_4@\text{SiO}_2\text{-N}_1$. The lowest binding percentage was found
504 in the case of $\text{Fe}_3\text{O}_4@\text{SiO}_2\text{-N}_2$ and $\text{Fe}_3\text{O}_4@\text{SiO}_2\text{-N}_1$ for Cd^{2+} at the level of 60% and 31%,
505 respectively. Moreover, the binding was not observed for Cd^{2+} and Pb^{2+} by $\text{Fe}_3\text{O}_4@\text{SiO}_2\text{-N}_3$
506 and for Pb^{2+} by $\text{Fe}_3\text{O}_4@\text{SiO}_2\text{-N}_3$. The obtained results show that the nanoparticles with three
507 amino groups in the outer chain — $\text{Fe}_3\text{O}_4@\text{SiO}_2\text{-N}_3$ — bind Cu^{2+} with high selectivity.

508 Furthermore, we used the adsorption and desorption experiment to analyse the Cu^{2+}
509 binding selectivity of $\text{Fe}_3\text{O}_4@\text{SiO}_2\text{-N}_3$. The obtained results directly indicate that the recovery
510 of Cu^{2+} from the aqueous solution is very high and reached 99.9%.

511 Examined series of amino functionalised $\text{Fe}_3\text{O}_4@\text{SiO}_2\text{-N}_n$ nanoparticles are promising
512 metal ion nano-adsorbents due to their high ion capacity, easy separation using magnetic field,
513 and renewability based on the pH value control.

514

515 **5. Acknowledgements**

516 This study was financed by the University of Gdansk within the project supporting young
517 scientists and PhD students (grant No. BMN 539-8210-B281-18 and 539-8210-B281-19).
518 Authors are grateful to Alexander Company Gdynia for a technical support.

519

520

521 **6. References**

522

- 523 [1] N.K. Srivastava, C.B. Majumder, Novel biofiltration methods for the treatment of heavy
524 metals from industrial wastewater, *Journal of Hazardous Materials*. 151 (2008) 1–8.
525 <https://doi.org/10.1016/j.jhazmat.2007.09.101>.
- 526 [2] M. Noreen, M. Shahid, M. Iqbal, J. Nisar, Measurement of cytotoxicity and heavy metal
527 load in drains water receiving textile effluents and drinking water in vicinity of drains,
528 *Measurement*. 109 (2017) 88–99. <https://doi.org/10.1016/j.measurement.2017.05.030>.
- 529 [3] H.S. Kim, Y.J. Kim, Y.R. Seo, An Overview of Carcinogenic Heavy Metal: Molecular
530 Toxicity Mechanism and Prevention, *Journal of Cancer Prevention*. 20 (2015) 232–240.
531 <https://doi.org/10.15430/JCP.2015.20.4.232>.
- 532 [4] H. Fu, P. Boffetta, Cancer and occupational exposure to inorganic lead compounds: a
533 meta-analysis of published data., *Occupational and Environmental Medicine*. 52 (1995)
534 73–81. <https://doi.org/10.1136/oem.52.2.73>.
- 535 [5] P. Joseph, Mechanisms of cadmium carcinogenesis, *Toxicology and Applied*
536 *Pharmacology*. 238 (2009) 272–279. <https://doi.org/10.1016/j.taap.2009.01.011>.
- 537 [6] E.K. Silbergeld, M. Waalkes, J.M. Rice, Lead as a carcinogen: Experimental evidence and
538 mechanisms of action, *American Journal of Industrial Medicine*. 38 (2000) 316–323.
539 [https://doi.org/10.1002/1097-0274\(200009\)38:3<316::AID-AJIM11>3.0.CO;2-P](https://doi.org/10.1002/1097-0274(200009)38:3<316::AID-AJIM11>3.0.CO;2-P).
- 540 [7] E.K. Silbergeld, Facilitative mechanisms of lead as a carcinogen, *Mutation*
541 *Research/Fundamental and Molecular Mechanisms of Mutagenesis*. 533 (2003) 121–133.
542 <https://doi.org/10.1016/j.mrfmmm.2003.07.010>.
- 543 [8] V.N. Bulut, H. Demirci, D. Ozdes, A. Gundogdu, O. Bekircan, M. Soylak, C. Duran, A
544 novel carrier element-free co-precipitation method for separation/preconcentration of lead
545 and cadmium ions from environmental matrices, *Environmental Progress & Sustainable*
546 *Energy*. 35 (2016) 1709–1715. <https://doi.org/10.1002/ep.12422>.
- 547 [9] X. Tang, H. Zheng, H. Teng, Y. Sun, J.-S. Guo, W. Xie, Q. Yang, W. Chen, Chemical
548 coagulation process for the removal of heavy metals from water: a review, *Desalination*
549 *and Water Treatment*. 57 (2014) 1–16. <https://doi.org/10.1080/19443994.2014.977959>.
- 550 [10] S.E. GHAZY, Separation of Cadmium(II) from Aqueous Solutions by the Precipitate
551 Flotation Technique, *Separation Science and Technology*. 29 (1994) 935–941.
552 <https://doi.org/10.1080/01496399408006637>.
- 553 [11] M.H. Salmani, M. Davoodi, M.H. Ehrampoush, M.T. Ghaneian, M.H. Fallahzadah,
554 Removal of cadmium (II) from simulated wastewater by ion flotation technique, *Iranian J*
555 *Environ Health Sci Eng*. 10 (2013) 16–20. <https://doi.org/10.1186/1735-2746-10-16>.
- 556 [12] J.B. Melville, E. Matijevic, Removal of copper, lead, and cadmium ions by microflotation,
557 *Journal of Colloid and Interface Science*. 57 (1976) 94–103.
558 [https://doi.org/10.1016/0021-9797\(76\)90179-X](https://doi.org/10.1016/0021-9797(76)90179-X).

- 559 [13] H. Abu-Qudais, H. Moussa, Removal of Heavy Metals from Wastewater by Membrane
560 Processes: A Comparative Study, *Desalination*. 164 (2004) 105–110.
561 [https://doi.org/10.1016/S0011-9164\(04\)00169-9](https://doi.org/10.1016/S0011-9164(04)00169-9).
- 562 [14] J. Kheriji, D. Tabassi, B. Hamrouni, Removal of Cd(II) ions from aqueous solution and
563 industrial effluent using reverse osmosis and nanofiltration membranes, *Water Sci
564 Technol*. 72 (2015) 1206–1216. <https://doi.org/10.2166/wst.2015.326>.
- 565 [15] A.P. de los Ríos, F.J. Hernández-Fernández, L.J. Lozano, S. Sánchez, J.I. Moreno, C.
566 Godínez, Removal of Metal Ions from Aqueous Solutions by Extraction with Ionic
567 Liquids, *J. Chem. Eng. Data*. 55 (2010) 605–608. <https://doi.org/10.1021/je9005008>.
- 568 [16] G.K. Sarma, S. Sen Gupta, K.G. Bhattacharyya, Nanomaterials as versatile adsorbents for
569 heavy metal ions in water: a review, *Environmental Science and Pollution Research*. 26
570 (2019) 6245–6278. <https://doi.org/10.1007/s11356-018-04093-y>.
- 571 [17] S.H. Khorzughy, T. Eslamkish, F.D. Ardejani, M.R. Heydartaemeh, Cadmium removal
572 from aqueous solutions by pumice and nano-pumice, *Korean Journal of Chemical
573 Engineering*. 32 (2015) 88–96. <https://doi.org/10.1007/s11814-014-0168-2>.
- 574 [18] W.-R. Lim, S.W. Kim, C.-H. Lee, E.-K. Choi, M.H. Oh, S.N. Seo, H.-J. Park, S.-Y.
575 Hamm, Performance of composite mineral adsorbents for removing Cu, Cd, and Pb ions
576 from polluted water, *Scientific Reports*. 9 (2019) 1–10.
577 <https://doi.org/10.1038/s41598-019-49857-9>.
- 578 [19] R. Wang, R. Liang, T. Dai, J. Chen, X. Shuai, C. Liu, Pectin-based adsorbents for heavy
579 metal ions: A review, *Trends in Food Science & Technology*. 91 (2019) 319–329.
580 <https://doi.org/10.1016/j.tifs.2019.07.033>.
- 581 [20] J. Li, X. Wang, G. Zhao, C. Chen, Z. Chai, A. Alsaedi, T. Hayat, X. Wang, Metal–organic
582 framework-based materials: superior adsorbents for the capture of toxic and radioactive
583 metal ions, *Chemical Society Reviews*. 47 (2018) 2322–2356.
584 <https://doi.org/10.1039/C7CS00543A>.
- 585 [21] S. Abdulrazak, K. Hussaini, H.M. Sani, Evaluation of removal efficiency of heavy metals
586 by low-cost activated carbon prepared from African palm fruit, *Applied Water Science*. 7
587 (2017) 3151–3155. <https://doi.org/10.1007/s13201-016-0460-x>.
- 588 [22] L. Wang, Y. Wang, F. Ma, V. Tankpa, S. Bai, X. Guo, X. Wang, Mechanisms and
589 reutilization of modified biochar used for removal of heavy metals from wastewater: A
590 review, *Science of The Total Environment*. 668 (2019) 1298–1309.
591 <https://doi.org/10.1016/j.scitotenv.2019.03.011>.
- 592 [23] S.S. Fiyadh, M.A. AlSaadi, W.Z. Jaafar, M.K. AlOmar, S.S. Fayaed, N.S. Mohd, L.S. Hin,
593 A. El-Shafie, Review on heavy metal adsorption processes by carbon nanotubes, *Journal
594 of Cleaner Production*. 230 (2019) 783–793.
595 <https://doi.org/10.1016/j.jclepro.2019.05.154>.
- 596 [24] W. Peng, H. Li, Y. Liu, S. Song, A review on heavy metal ions adsorption from water by
597 graphene oxide and its composites, *Journal of Molecular Liquids*. 230 (2017) 496–504.
598 <https://doi.org/10.1016/j.molliq.2017.01.064>.
- 599 [25] Y. He, P. Wu, W. Xiao, G. Li, J. Yi, Y. He, C. Chen, P. Ding, Y. Duan, Efficient removal
600 of Pb(II) from aqueous solution by a novel ion imprinted magnetic biosorbent: Adsorption
601 kinetics and mechanisms, *PLOS ONE*. 14 (2019) e0213377 (1-17).
602 <https://doi.org/10.1371/journal.pone.0213377>.
- 603 [26] I. Hasan, R.A. Khan, W. Alharbi, K.H. Alharbi, A. Alsalmeh, In Situ Copolymerized
604 Polyacrylamide Cellulose Supported Fe₃O₄ Magnetic Nanocomposites for Adsorptive
605 Removal of Pb(II): Artificial Neural Network Modeling and Experimental Studies,
606 *Nanomaterials*. 9 (2019) 1687. <https://doi.org/10.3390/nano9121687>.

- 607 [27] V. Nejadshafiee, M.R. Islami, Adsorption capacity of heavy metal ions using sultone-
608 modified magnetic activated carbon as a bio-adsorbent, *Materials Science and*
609 *Engineering: C*. 101 (2019) 42–52. <https://doi.org/10.1016/j.msec.2019.03.081>.
- 610 [28] N.T. Abdel-Ghani, G.A. El-Chaghaby, E.-S.A. Rawash, E.C. Lima, Magnetic activated
611 carbon nanocomposite from *Nigella sativa* L. waste (MNSA) for the removal of
612 Coomassie brilliant blue dye from aqueous solution: Statistical design of experiments for
613 optimization of the adsorption conditions, *Journal of Advanced Research*. 17 (2019)
614 55–63. <https://doi.org/10.1016/j.jare.2018.12.004>.
- 615 [29] Y. Ji, C. Ma, J. Li, H. Zhao, Q. Chen, M. Li, H. Liu, A Magnetic Adsorbent for the
616 Removal of Cationic Dyes from Wastewater, *Nanomaterials*. 8 (2018) 710 (1–13).
617 <https://doi.org/10.3390/nano8090710>.
- 618 [30] C. Jiang, X. Wang, D. Qin, W. Da, B. Hou, C. Hao, J. Wu, Construction of magnetic
619 lignin-based adsorbent and its adsorption properties for dyes, *Journal of Hazardous*
620 *Materials*. 369 (2019) 50–61. <https://doi.org/10.1016/j.jhazmat.2019.02.021>.
- 621 [31] E. Ghasemi, A. Heydari, M. Sillanpää, Superparamagnetic Fe₃O₄@EDTA nanoparticles
622 as an efficient adsorbent for simultaneous removal of Ag(I), Hg(II), Mn(II), Zn(II), Pb(II)
623 and Cd(II) from water and soil environmental samples, *Microchemical Journal*. 131
624 (2017) 51–56. <https://doi.org/10.1016/j.microc.2016.11.011>.
- 625 [32] S. Bao, L. Tang, K. Li, P. Ning, J. Peng, H. Guo, T. Zhu, Y. Liu, Highly selective removal
626 of Zn(II) ion from hot-dip galvanizing pickling waste with amino-functionalized Fe₃O₄
627 @SiO₂ magnetic nano-adsorbent, *Journal of Colloid and Interface Science*. 462 (2016)
628 235–242. <https://doi.org/10.1016/j.jcis.2015.10.011>.
- 629 [33] A. Dolgormaa, C. Lv, Y. Li, J. Yang, J. Yang, P. Chen, H. Wang, J. Huang, Adsorption
630 of Cu(II) and Zn(II) Ions from Aqueous Solution by Gel/PVA-Modified Super-
631 Paramagnetic Iron Oxide Nanoparticles, *Molecules*. 23 (2018) 2982–2997.
632 <https://doi.org/10.3390/molecules23112982>.
- 633 [34] H. Zheng, L. Zhou, Z. Liu, Z. Le, J. Ouyang, G. Huang, H. Shehzad, Functionalization of
634 mesoporous Fe₃O₄@SiO₂ nanospheres for highly efficient U(VI) adsorption,
635 *Microporous and Mesoporous Materials*. 279 (2019) 316–322.
636 <https://doi.org/10.1016/j.micromeso.2018.12.038>.
- 637 [35] A. Tadjarodi, A. Abbaszadeh, M. Taghizadeh, N. Shekari, A.A. Asgharinezhad, Solid
638 phase extraction of Cd(II) and Pb(II) ions based on a novel functionalized Fe₃O₄@ SiO₂
639 core-shell nanoparticles with the aid of multivariate optimization methodology, *Materials*
640 *Science and Engineering: C*. 49 (2015) 416–421.
641 <https://doi.org/10.1016/j.msec.2015.01.013>.
- 642 [36] F. Mohammadi, F. Mohammadi, A. Esrafil, H.R. Sobhi, M. Behbahani, M. Kermani, E.
643 Asgari, Z.R. Fasih, Evaluation of adsorption and removal of methylparaben from aqueous
644 solutions using amino-functionalized magnetic nanoparticles as an efficient adsorbent:
645 Optimization and modeling by response surface methodology (RSM), *DESALINATION*
646 *AND WATER TREATMENT*. 103 (2018) 248–260.
647 <https://doi.org/10.5004/dwt.2018.21781>.
- 648 [37] A. Sheikhmohammadi, Z. Dahaghin, S.M. Mohseni, M. Sarkhosh, H. Azarpira, Z. Atafar,
649 M. Abtahi, S. Rezaei, M. Sardar, H. Masoudi, M. Faraji, S. Nazari, R.H. Pouya, M.
650 Almasian, The synthesis and application of the SiO₂@Fe₃O₄@MBT nanocomposite
651 as a new magnetic sorbent for the adsorption of arsenate from aqueous solutions:
652 Modeling, optimization, and adsorption studies, *Journal of Molecular Liquids*. 255 (2018)
653 313–323. <https://doi.org/10.1016/j.molliq.2018.01.164>.
- 654 [38] A. Sheikhmohammadi, M. Safari, A. Alinejad, A. Esrafil, H. Nourmoradi, E. Asgari, The
655 synthesis and application of the Fe₃O₄@SiO₂ nanoparticles functionalized with
656 3-aminopropyltriethoxysilane as an efficient sorbent for the adsorption of Ethylparaben

- 657 from wastewater: synthesis, kinetic, thermodynamic and equilibrium studies, *Journal of*
658 *Environmental Chemical Engineering*. 7 (2019) 103315 (1–9).
659 <https://doi.org/10.1016/j.jece.2019.103315>.
- 660 [39] R. Roto, Y. Yusran, A. Kuncaka, Magnetic adsorbent of Fe₃O₄@SiO₂ core-shell
661 nanoparticles modified with thiol group for chloroauric ion adsorption, *Applied Surface*
662 *Science*. 377 (2016) 30–36. <https://doi.org/10.1016/j.apsusc.2016.03.099>.
- 663 [40] F. Ghorbani, S. Kamari, Core-shell magnetic nanocomposite of Fe₃O₄@SiO₂@NH₂ as
664 an efficient and highly recyclable adsorbent of methyl red dye from aqueous
665 environments, *Environmental Technology & Innovation*. 14 (2019) 100333 (1–16).
666 <https://doi.org/10.1016/j.eti.2019.100333>.
- 667 [41] S. De Gisi, G. Lofrano, M. Grassi, M. Notarnicola, Characteristics and adsorption
668 capacities of low-cost sorbents for wastewater treatment: A review, *Sustainable Materials*
669 *and Technologies*. 9 (2016) 10–40. <https://doi.org/10.1016/j.susmat.2016.06.002>.
- 670 [42] J. Wang, S. Zheng, Y. Shao, J. Liu, Z. Xu, D. Zhu, Amino-functionalized Fe₃O₄@SiO₂
671 core-shell magnetic nanomaterial as a novel adsorbent for aqueous heavy metals removal,
672 *Journal of Colloid and Interface Science*. 349 (2010) 293–299.
673 <https://doi.org/10.1016/j.jcis.2010.05.010>.
- 674 [43] L. Sun, S. Hu, H. Sun, H. Guo, H. Zhu, M. Liu, H. Sun, Malachite green Adsorption onto
675 Fe₃O₄@SiO₂-NH₂: Isotherms, Kinetic and Process Optimization, *RSC Advances*. (2012)
676 11837–11844.
- 677 [44] M. Hanif, C.G. Hartinger, Anticancer metallodrugs: where is the next cisplatin?, *Future*
678 *Medicinal Chemistry*. 10 (2018) 615–617. <https://doi.org/10.4155/fmc-2017-0317>.
- 679 [45] T. Lazarević, A. Rilak, Ž.D. Bugarčić, Platinum, palladium, gold and ruthenium
680 complexes as anticancer agents: Current clinical uses, cytotoxicity studies and future
681 perspectives, *European Journal of Medicinal Chemistry*. 142 (2017) 8–31.
682 <https://doi.org/10.1016/j.ejmech.2017.04.007>.
- 683 [46] P. Ferenci, Diagnosis of Wilson disease, in: *Handbook of Clinical Neurology*, Elsevier,
684 2017: pp. 171–180. <https://doi.org/10.1016/B978-0-444-63625-6.00014-8>.
- 685 [47] P.C. Panta, C.P. Bergmann, Obtention by Coprecipitation and Magnetic Characterization
686 of Fe₃O₄ Nanoparticles Coated with Surfactants, *Nano Research & Applications*. 1 (2015)
687 1–4.
- 688 [48] D.K. Kim, M. Mikhaylova, Y. Zhang, M. Muhammed, Protective Coating of
689 Superparamagnetic Iron Oxide Nanoparticles, *Chemistry of Materials*. 15 (2003)
690 1617–1627. <https://doi.org/10.1021/cm021349j>.
- 691 [49] Z. Lu, J. Dai, X. Song, G. Wang, W. Yang, Facile synthesis of Fe₃O₄/SiO₂ composite
692 nanoparticles from primary silica particles, *Colloids and Surfaces A: Physicochemical and*
693 *Engineering Aspects*. 317 (2008) 450–456.
694 <https://doi.org/10.1016/j.colsurfa.2007.11.020>.
- 695 [50] D. Dupont, J. Luyten, M. Bloemen, T. Verbiest, K. Binnemans, Acid-Stable Magnetic
696 Core-Shell Nanoparticles for the Separation of Rare Earths, *Industrial & Engineering*
697 *Chemistry Research*. 53 (2014) 15222–15229. <https://doi.org/10.1021/ie502546c>.
- 698 [51] G.H. Bogush, C.F. Zukoski, Studies of the kinetics of the precipitation of uniform silica
699 particles through the hydrolysis and condensation of silicon alkoxides, *Journal of Colloid*
700 *and Interface Science*. 142 (1991) 1–18. [https://doi.org/10.1016/0021-9797\(91\)90029-8](https://doi.org/10.1016/0021-9797(91)90029-8).
- 701 [52] Y.A. Barnakov, M.H. Yu, Z. Rosenzweig, Manipulation of the Magnetic Properties of
702 Magnetite-Silica Nanocomposite Materials by Controlled Stober Synthesis, *Langmuir*. 21
703 (2005) 7524–7527. <https://doi.org/10.1021/la0508893>.
- 704 [53] M. Zhu, M.Z. Lerum, W. Chen, How To Prepare Reproducible, Homogeneous, and
705 Hydrolytically Stable Aminosilane-Derived Layers on Silica, *Langmuir*. 28 (2012)
706 416–423. <https://doi.org/10.1021/la203638g>.

- 707 [54] E.T. Vandenberg, L. Bertilsson, B. Liedberg, K. Uvdal, R. Erlandsson, H. Elwing, I.
708 Lundström, Structure of 3-aminopropyl triethoxy silane on silicon oxide, *Journal of*
709 *Colloid and Interface Science.* 147 (1991) 103–118.
710 [https://doi.org/10.1016/0021-9797\(91\)90139-Y](https://doi.org/10.1016/0021-9797(91)90139-Y).
- 711 [55] A. Bayat, M. Shakourian-Fard, N. Ehyaei, M.M. Hashemi, A magnetic supported iron
712 complex for selective oxidation of sulfides to sulfoxides using 30% hydrogen peroxide at
713 room temperature, *RSC Adv.* 4 (2014) 44274–44281.
714 <https://doi.org/10.1039/C4RA07356H>.
- 715 [56] P. Arévalo-Cid, J. Isasi, F. Martín-Hernández, Comparative study of core-shell
716 nanostructures based on amino-functionalized Fe₃O₄@SiO₂ and CoFe₂O₄@SiO₂
717 nanocomposites, *Journal of Alloys and Compounds.* 766 (2018) 609–618.
718 <https://doi.org/10.1016/j.jallcom.2018.06.246>.
- 719 [57] H. Ciftci, B. Ersoy, A. Evcin, Synthesis, Characterization and Cr(VI) Adsorption
720 Properties of Modified Magnetite Nanoparticles, *Acta Physica Polonica A.* 132 (2017)
721 564–569. <https://doi.org/10.12693/APhysPolA.132.564>.
- 722 [58] A. Kulpa, J. Ryl, G. Skowierzak, A. Koterwa, G. Schroeder, T. Ossowski, P.
723 Niedziałkowski, Comparison of Cadmium Cd²⁺ and Lead Pb²⁺ Binding by
724 Fe₂O₃@SiO₂-EDTA Nanoparticles – Binding Stability and Kinetic Studies,
725 *Electroanalysis.* 32 (2020) 588–597. <https://doi.org/10.1002/elan.201900616>.
- 726 [59] Y. Liu, R. Fu, Y. Sun, X. Zhou, S.A. Baig, X. Xu, Multifunctional nanocomposites Fe₃
727 O₄@SiO₂-EDTA for Pb(II) and Cu(II) removal from aqueous solutions, *Applied*
728 *Surface Science.* 369 (2016) 267–276. <https://doi.org/10.1016/j.apsusc.2016.02.043>.
- 729 [60] S. Jin, B.C. Park, W.S. Ham, L. Pan, Y.K. Kim, Effect of the magnetic core size of amino-
730 functionalized Fe₃O₄-mesoporous SiO₂ core-shell nanoparticles on the removal of heavy
731 metal ions, *Colloids and Surfaces A: Physicochemical and Engineering Aspects.* 531
732 (2017) 133–140. <https://doi.org/10.1016/j.colsurfa.2017.07.086>.
- 733 [61] F. Liu, F. Niu, N. Peng, Y. Su, Y. Yang, Synthesis, characterization, and application of
734 Fe₃O₄@SiO₂-NH₂ nanoparticles, *RSC Adv.* 5 (2015) 18128–18136.
735 <https://doi.org/10.1039/C4RA15968C>.
- 736 [62] Y. Zhu, Y. Fang, S. Kaskel, Folate-Conjugated Fe₃O₄@SiO₂ Hollow Mesoporous
737 Spheres for Targeted Anticancer Drug Delivery, *The Journal of Physical Chemistry C.*
738 114 (2010) 16382–16388. <https://doi.org/10.1021/jp106685q>.
- 739 [63] S. Shi, J. Yang, S. Liang, M. Li, Q. Gan, K. Xiao, J. Hu, Enhanced Cr(VI) removal from
740 acidic solutions using biochar modified by Fe₃O₄@SiO₂-NH₂ particles, *Sci. Total*
741 *Environ.* 628–629 (2018) 499–508. <https://doi.org/10.1016/j.scitotenv.2018.02.091>.
- 742 [64] M.E. Khosroshahi, L. Ghazanfari, Synthesis and functionalization of SiO₂ coated Fe₃O₄
743 nanoparticles with amine groups based on self-assembly, *Materials Science and*
744 *Engineering: C.* 32 (2012) 1043–1049. <https://doi.org/10.1016/j.msec.2011.09.003>.
- 745 [65] P.M. Dietrich, S. Glamsch, C. Ehlert, A. Lippitz, N. Kulak, W.E.S. Unger, Synchrotron-
746 radiation XPS analysis of ultra-thin silane films: Specifying the organic silicon, *Applied*
747 *Surface Science.* 363 (2016) 406–411. <https://doi.org/10.1016/j.apsusc.2015.12.052>.
- 748 [66] High Resolution XPS of Organic Polymers: The Scienta ESCA300 Database (Beamson,
749 G.; Briggs, D.), *J. Chem. Educ.* 70 (1993) A25. <https://doi.org/10.1021/ed070pA25.5>.
- 750 [67] S.R. Darmakkolla, H. Tran, A. Gupta, S.B. Rananavare, A method to derivatize surface
751 silanol groups to Si-alkyl groups in carbon-doped silicon oxides, *RSC Adv.* 6 (2016)
752 93219–93230. <https://doi.org/10.1039/C6RA20355H>.
- 753 [68] A.K. Chauhan, D.K. Aswal, S.P. Koiry, S.K. Gupta, J.V. Yakhmi, C. Sürgers, D. Guerin,
754 S. Lenfant, D. Vuillaume, Self-assembly of the 3-aminopropyltrimethoxysilane
755 multilayers on Si and hysteretic current–voltage characteristics, *Appl. Phys. A.* 90 (2008)
756 581–589. <https://doi.org/10.1007/s00339-007-4336-7>.

- 757 [69] N. Graf, E. Yegen, T. Gross, A. Lippitz, W. Weigel, S. Krakert, A. Terfort, W.E.S. Unger,
758 XPS and NEXAFS studies of aliphatic and aromatic amine species on functionalized
759 surfaces, *Surface Science*. 603 (2009) 2849–2860.
760 <https://doi.org/10.1016/j.susc.2009.07.029>.
- 761 [70] A. Elhambakhsh, P. Keshavarz, Investigation of Carbon Dioxide Absorption Using
762 Different Functionalized Fe₃O₄ Magnetic Nanoparticles, *Energy Fuels*. (2020).
763 <https://doi.org/10.1021/acs.energyfuels.0c00234>.
- 764 [71] Q. Zhao, Y. Zhu, Z. Sun, Y. Li, G. Zhang, F. Zhang, X. Fan, Combining palladium
765 complex and organic amine on graphene oxide for promoted Tsuji–Trost allylation, *J.*
766 *Mater. Chem. A*. 3 (2015) 2609–2616. <https://doi.org/10.1039/C4TA05205F>.
- 767 [72] T.L. Barr, S. Seal, Nature of the use of adventitious carbon as a binding energy standard,
768 *Journal of Vacuum Science & Technology A: Vacuum, Surfaces, and Films*. 13 (1995)
769 1239–1246. <https://doi.org/10.1116/1.579868>.
- 770 [73] R. Bogdanowicz, M. Sawczak, P. Niedzialkowski, P. Zieba, B. Finke, J. Ryl, J.
771 Karczewski, T. Ossowski, Novel Functionalization of Boron-Doped Diamond by
772 Microwave Pulsed-Plasma Polymerized Allylamine Film, *J. Phys. Chem. C*. 118 (2014)
773 8014–8025. <https://doi.org/10.1021/jp5003947>.
- 774 [74] P. Niedzialkowski, R. Bogdanowicz, P. Zięba, J. Wysocka, J. Ryl, M. Sobaszek, T.
775 Ossowski, Melamine-modified Boron-doped Diamond towards Enhanced Detection of
776 Adenine, Guanine and Caffeine, *Electroanalysis*. 28 (2016) 211–221.
777 <https://doi.org/10.1002/elan.201500528>.
- 778 [75] F. Mirabella, E. Zaki, F. Ivars-Barcelo, S. Schaueremann, S. Shaikhutdinov, H.-J. Freund,
779 CO₂ Adsorption on Magnetite Fe₃O₄(111), *J. Phys. Chem. C*. 122 (2018) 27433–27441.
780 <https://doi.org/10.1021/acs.jpcc.8b08240>.
- 781 [76] J. Pavelec, J. Hulva, D. Halwidl, R. Bliem, O. Gamba, Z. Jakub, F. Brunbauer, M. Schmid,
782 U. Diebold, G.S. Parkinson, A multi-technique study of CO₂ adsorption on Fe₃O₄
783 magnetite, *J. Chem. Phys.* 146 (2017) 014701 (1)-014701 (10).
784 <https://doi.org/10.1063/1.4973241>.
- 785 [77] T. Yang, J. Liu, Y. Wang, X. Wen, B. Shen, Structures and energetics of CO₂ adsorption
786 on the Fe₃O₄ (111) surface, *Journal of Fuel Chemistry and Technology*. 46 (2018) 1113–
787 1120. [https://doi.org/10.1016/S1872-5813\(18\)30044-6](https://doi.org/10.1016/S1872-5813(18)30044-6).
- 788 [78] F. Bai, X. Zhang, X. Hou, H. Liu, J. Chen, T. Yang, Individual and Simultaneous
789 Voltammetric Determination of Cd(II), Cu(II) and Pb(II) Applying Amino Functionalized
790 Fe₃O₄@Carbon Microspheres Modified Electrode, *Electroanalysis*. 31 (2019) 1448–
791 1457. <https://doi.org/10.1002/elan.201900234>.
- 792 [79] A. Profumo, D. Merli, M. Pesavento, Voltammetric determination of inorganic As(III) and
793 total inorganic As in natural waters, *Analytica Chimica Acta*. 539 (2005) 245–250.
794 <https://doi.org/10.1016/j.aca.2005.02.062>.
- 795 [80] N. Kataria, V.K. Garg, Green synthesis of Fe₃O₄ nanoparticles loaded sawdust carbon for
796 cadmium (II) removal from water: Regeneration and mechanism, *Chemosphere*. 208
797 (2018) 818–828. <https://doi.org/10.1016/j.chemosphere.2018.06.022>.
- 798 [81] W.H.M. Abdelraheem, Z.R. Komy, N.M. Ismail, Electrochemical determination of Cu²⁺
799 complexation in the extract of *E. crassipes* by anodic stripping voltammetry, *Arabian*
800 *Journal of Chemistry*. 10 (2017) S1105–S1110.
801 <https://doi.org/10.1016/j.arabjc.2013.01.019>.
- 802 [82] W. Nowicki, Structural studies of complexation of Cu(II) with aminosilane-modified
803 silica surface in heterogeneous system in a wide range of pH, *Applied Surface Science*.
804 469 (2019) 566–572. <https://doi.org/10.1016/j.apsusc.2018.11.066>.
- 805 [83] S.E. Lehman, I.A. Mudunkotuwa, V.H. Grassian, S.C. Larsen, Nano–Bio Interactions of
806 Porous and Nonporous Silica Nanoparticles of Varied Surface Chemistry: A Structural,

- 807 Kinetic, and Thermodynamic Study of Protein Adsorption from RPMI Culture Medium,
808 Langmuir. 32 (2016) 731–742. <https://doi.org/10.1021/acs.langmuir.5b03997>.
- 809 [84] D. Chen, T. Awut, B. Liu, Y. Ma, T. Wang, I. Nurulla, Functionalized magnetic Fe₃O₄
810 nanoparticles for removal of heavy metal ions from aqueous solutions, E-Polymers. 4
811 (2016) 313–322. <https://doi.org/10.1515/epoly-2016-0043>.
- 812 [85] M. Sun, P. Li, X. Jin, X. Ju, W. Yan, J. Yuan, X. Changrui, Heavy metal adsorption onto
813 graphene oxide, amino group on magnetic nanoadsorbents and application for detection
814 of Pb(II) by strip sensor, Food and Agricultural Immunology. 29 (2018) 1053–1073.
815 <https://doi.org/10.1080/09540105.2018.1509946>.
- 816 [86] J. Zhang, S. Zhai, S. Li, Z. Xiao, Y. Song, Q. An, G. Tian, Pb(II) removal of
817 Fe₃O₄@SiO₂-NH₂ core-shell nanomaterials prepared via a controllable sol-gel process,
818 Chemical Engineering Journal. 215–216 (2013) 461–471.
819 <https://doi.org/10.1016/j.cej.2012.11.043>.
- 820 [87] X.L. Wu, D. Zhao, S.T. Yang, Impact of solution chemistry conditions on the sorption
821 behavior of Cu(II) on Lin'an montmorillonite, Desalination. 269 (2011) 84–91.
822 <https://doi.org/10.1016/j.desal.2010.10.046>.
- 823 [88] J. Vuceta, J.J. Morgan, Hydrolysis of Cu(II), Limnology and Oceanography. 22 (1977)
824 742–746. <https://doi.org/10.4319/lo.1977.22.4.0742>.
- 825
- 826